Research Square

Preprints are preliminary reports that have not undergone peer review.
They should not be considered conclusive, used to inform clinical practice,
or referenced by the media as validated information.

Multi-Source Analysis and WRF Data Assimilation Experiments for Hazardous Tropical Convection Producing Surface-Reaching Hail

Krisna Dwi Oktabrian
Sekolah Tinggi Meterorologi Klimatologi dan Geofisika
Adi Mulsandi
adi.mulsandi@stmkg.ac.id

Sekolah Tinggi Meterorologi Klimatologi dan Geofisika

Research Article

Keywords: tropical hail, surface-reaching hail, hazardous tropical convection, WRFDA-3DVAR, radar reflectivity assimilation, hail-supporting proxy

Posted Date: June 1st, 2026

DOI: https://doi.org/10.21203/rs.3.rs-9641225/v1

License: This work is licensed under a Creative Commons Attribution 4.0 International License.
Read Full License

Additional Declarations: No competing interests reported.

Version of Record: A version of this preprint was published at Modeling Earth Systems and Environment on October 8th, 2026. See the published version at https://doi.org/10.1007/s40808-026-02937-y.

Multi-Source Analysis and WRF Data Assimilation Experiments for Hazardous Tropical Convection Producing Surface-Reaching Hail

Abstract

Surface-reaching hail in the humid tropics is a rare but hazardous manifestation of deep convection, as hailstones must survive descent through a deep warm layer and high melting-level environment. This study investigates hazardous tropical convection producing surface-reaching hail over Yogyakarta, Indonesia, on 11 March 2025, using surface hail reports, Semarang radar observations, Himawari-9 infrared brightness temperature, sounding and ERA5 diagnostics, and WRF data assimilation experiments using WRFDA-3DVAR. A synthetic reflectivity-based hail-supporting proxy was developed from WRF hydrometeor fields, and storm representation was assessed using object-based and spatial metrics, including structure–amplitude–location, distance error, hit rate, intersection-over-union, and fractions skill score. Observations showed rapid convective intensification between 08:00 and 08:20 UTC, closely coinciding with the reported hail occurrence at approximately 08:15 UTC. Himawari-9 indicated cloud-top cooling from approximately −53°C to −72°C within 20 min, while environmental diagnostics showed moderate-to-strong instability, weak inhibition, a high freezing level, and organized low-level convergence. Among the assimilation experiments, radar reflectivity assimilation produced the most physically consistent storm-object representation, with the lowest total SAL value and distance error, whereas all-source assimilation increased hit rate but degraded storm-object compactness. These findings demonstrate that surface-reaching tropical hail should be interpreted as an indicator of hazardous convection and that WRF data assimilation experiments, combined with object-based verification, can improve the evaluation of compact hail-supporting storm cores.

Keywords: tropical hail; surface-reaching hail; hazardous tropical convection; WRFDA-3DVAR; radar reflectivity assimilation; hail-supporting proxy.

1. Introduction

Surface-reaching hail in humid tropical environments is rare [1]–[6] yet it is scientifically important because it indicates severe deep convection capable of overcoming high freezing levels and deep melting layers [3], [7]–[9]. Unlike many mid-latitude hailstorms, which are commonly associated with strong vertical wind shear, rotating updrafts, and organized supercell dynamics, tropical hail often develops in warm, moist environments with weak-to-moderate vertical shear [1], [4], [10]. Under these conditions, hail observed at the surface reflects not only ice formation aloft but also strong updrafts, mixed-phase hydrometeor growth, hydrometeor loading, and rapid downward transport through a deep warm layer [11]–[15].

Despite its high-impact nature, surface-reaching tropical hail remains poorly documented compared with hail in mid-latitude severe-storm environments. This knowledge gap is important because tropical surface hail may represent a localized but hazardous manifestation of deep convective intensity rather than a routine outcome of ice formation aloft. Its diagnosis is challenging because no single observing system can fully capture the hail-producing process [16]–[31]. Radar observations provide information on the timing, intensity, and spatial organization of convective cores [32]–[36], satellite infrared observations indicate cloud-top cooling and rapid convective deepening [37]–[42], and surface reports provide direct evidence of hail reaching the ground. However, each data source has limitations, including ambiguity in radar reflectivity, the indirect nature of satellite inference, and uncertainty in the timing, location, and hailstone size reported at the surface. These limitations highlight the need for an integrated framework that combines surface reports, radar, satellite diagnostics, environmental analysis, and numerical modeling.

Numerical weather prediction models provide a physically consistent framework for examining hail-supporting convection because they resolve thermodynamic profiles, hydrometeor fields, vertical motion, and storm-scale structures [43]–[55]. However, convective-scale simulations remain sensitive to initial conditions, storm displacement errors, microphysical parameterizations, and mesoscale forcing. Data assimilation can reduce some of these uncertainties by incorporating observational constraints into the model state. Radar reflectivity assimilation directly constrains hydrometeor and precipitation structures, radial-velocity assimilation improves the representation of storm-scale kinematics, and satellite and conventional observations can improve cloud-field development and the pre-convective environment. Nevertheless, assimilating additional observation types does not necessarily improve the representation of hail-related storms, particularly when simulated convection becomes spatially overexpanded or structurally unrealistic.

Verification is therefore essential for determining whether data assimilation genuinely improves the representation of hail-supporting convection. Traditional grid-point verification may penalize physically plausible simulations when storm objects are displaced by only a few kilometers, whereas simple overlap or hit-rate metrics may overestimate skill when simulations produce unrealistically broad hail-supporting areas. Object-based verification is more appropriate for localized convective hazards because it evaluates storm morphology, intensity,

location, and spatial overlap simultaneously. This approach is particularly important for tropical surface-reaching hail, which is short-lived, spatially compact, and sensitive to convective-scale displacement errors.

This study investigates a high-impact convective storm that produced surface-reaching hail over Yogyakarta, Indonesia, on 11 March 2025. This event provides a valuable case for examining the representation of tropical hail because surface hail reports were spatially clustered within radar coverage and coincided with rapid convective intensification. The analysis integrates surface hail reports, Semarang weather radar observations, Himawari-9 infrared brightness temperature, sounding diagnostics, ERA5 low-level wind and divergence fields, and WRF simulations using multiple data assimilation configurations. Because explicit hail or radar-reflectivity variables were unavailable from the WRF output, a synthetic reflectivity-based hail-supporting proxy was developed from model hydrometeor fields.

The novelty of this study lies in its integrated, object-based evaluation of WRF data assimilation experiments for hazardous tropical convection producing surface-reaching hail. Using multi-source observations, WRFDA-3DVAR experiments, a hydrometeor-based synthetic hail-supporting proxy, and multi-metric verification, this study evaluates how different assimilation strategies represent compact hail-supporting convective structures. Rather than treating hail prediction as a simple reflectivity-threshold problem, this study distinguishes among surface-observed hail, radar-derived hail-likelihood signatures, and model-derived hail-supporting convective proxies. In this framework, surface-reaching hail is treated as an indicator of hazardous tropical convection rather than as a standalone precipitation phenomenon. This distinction is critical in tropical environments, where surface hail depends on both ice-phase microphysics aloft and hailstone survival during descent through a deep warm layer.

The objectives of this study are threefold. First, the observed evolution and environmental conditions of hazardous tropical convection producing surface-reaching hail are reconstructed using surface reports, radar, satellite, sounding, and reanalysis data. Second, the effects of different data assimilation configurations on simulated storm morphology, intensity, and hail-supporting convective structures are examined. Third, object-based and spatial verification metrics, including structure–amplitude–location, distance error, hit rate, intersection-over-union, and fractions skill score, are used to quantify the strengths and limitations of each simulation experiment. Through this framework, this study assesses how different WRF data assimilation experiments represent compact hail-supporting convective structures associated with surface-reaching hail.

2. Data and Method

2.1 Study event and surface hail reports

This study focuses on a surface-reaching hail event associated with deep tropical convection over the Special Region of Yogyakarta, Indonesia, on 11 March 2025. Surface hail was reported at approximately 08:15 UTC, corresponding to 15:15 local time in Western Indonesia. The hailfall affected urban and peri-urban areas across Sleman Regency, Yogyakarta City, and Bantul Regency, with the densest reports clustered along the Sleman–Yogyakarta urban corridor, including the UGM campus area, Mlati, Depok, Gamping, Jalan Kaliurang, Jalan Magelang, Ngaglik, Tajem, and surrounding settlements.

Surface reports were used as the primary evidence that hail reached the ground, whereas radar reflectivity, satellite cloud-top temperature, and model-derived hail proxies were interpreted as hail-supporting storm signatures rather than direct observations of surface hailfall [15], [26], [56]–[64]. Although systematic hail-pad observations or instrumental hail-size measurements were unavailable, qualitative reports of gravel-like to coin-sized hailstones indicate that frozen hydrometeors were sufficiently large to survive descent through the warm tropical lower troposphere.

To account for uncertainty in community-based reports, hail observations were treated using a spatio-temporal matching framework rather than exact point verification. Each reported location was represented by an approximate centroid coordinate, with a ±30 min temporal window around the reported hail time, corresponding to 07:45–08:45 UTC, and a 3–5 km spatial buffer to account for uncertainty in reported position, storm displacement, radar sampling geometry, and model grid representation. Duplicate or closely overlapping reports were retained only when they represented distinct localities or independent spatial anchors within the hail-affected corridor, while reports of fallen trees, localized wind damage, and other storm-related impacts were used only as contextual evidence of severe convective conditions.

The spatial setting of the event, the position of the Semarang weather radar, and the distribution of reported hail locations are shown in **Figure 1**, while their representative coordinates are summarized in **Table 1**. These coordinates should be interpreted as approximate spatial anchors for event reconstruction and verification, not as exact hailfall boundaries.

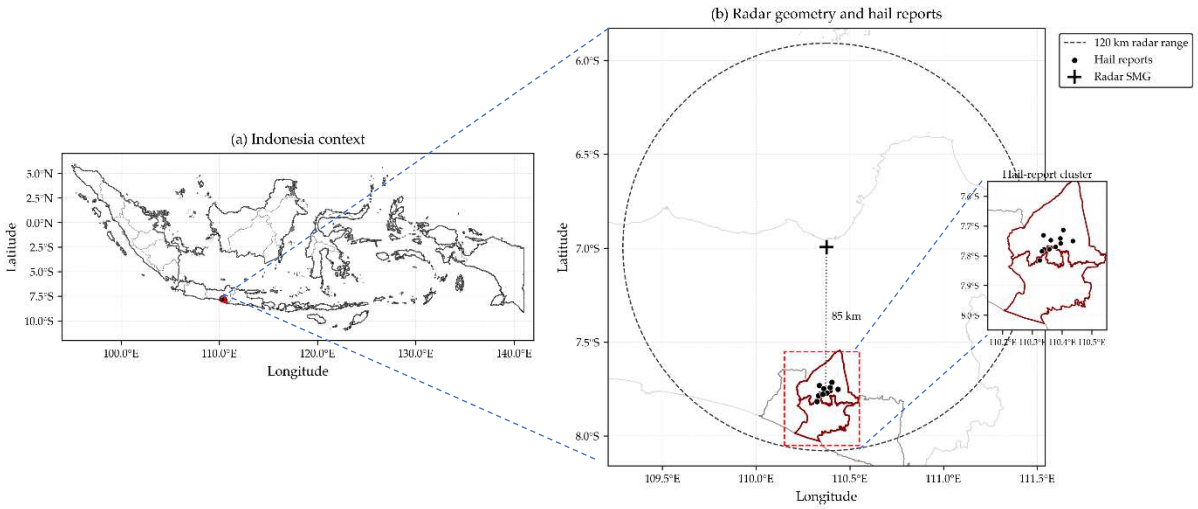


Figure 1. Geographic setting of the hail-producing convective event on 11 March 2025. (a) Location of the Special Region of Yogyakarta within Indonesia. (b) Spatial configuration of the Semarang weather radar, its approximate 120 km coverage range, and reported surface hail locations over Sleman, Yogyakarta City, and Bantul.

Table 1. Approximate representative coordinates of reported surface hail locations on 11 March 2025 over the Yogyakarta region. Coordinates represent approximate centroids of reported locations derived from BNPB/community-based field mapping and are used as spatial anchors for verification.

Hail Location	Regency / City	Subdistrict	Latitude	Longitude
Ringroad Barat	Sleman	Gamping/Mlati	-7.77770	110.33898
Ngaglik	Sleman	Ngaglik	-7.71346	110.40389
Tajem	Sleman	Ngemplak	-7.75056	110.43600
Mlati	Sleman	Mlati	-7.73063	110.33684
Depok	Sleman	Depok	-7.75869	110.39470
Gamping	Sleman	Gamping	-7.78431	110.33221
Jalan Kaliurang	Sleman	Ngaglik–Depok	-7.74200	110.39400
Jalan Magelang	Sleman and Yogyakarta	Mlati–Tegalrejo	-7.74700	110.36100
Balairung UGM	Sleman	Depok	-7.7704	110.3778
Kemantren Tegalrejo	Yogyakarta	Tegalrejo	-7.77806	110.35611
Kasihan	Bantul	Kasihan	-7.81560	110.32416

2.2 Radar observations and radar-based hail likelihood

Radar observations from the Semarang weather radar were used to examine the timing, intensity, spatial structure, and evolution of the hail-producing convective storm. The radar is located at 6.993198°S and 110.375514°E, with an antenna height of approximately 74 m above mean sea level. The reported hail cluster over Yogyakarta was approximately 84 km south of the radar site and remained within the nominal radar coverage range. Composite maximum reflectivity was analyzed at 10-min intervals from 07:20 to 08:40 UTC, covering the pre-intensification, rapid-growth, mature, and early weakening stages, including the reported surface hail occurrence at approximately 08:15 UTC.

The Semarang radar volume scan consisted of multiple elevation angles, including 0.5°, 1.5°, 2.4°, 3.5°, 4.3°, 6.0°, 9.9°, 14.6°, 19.0°, 25.0°, and 45.0°. At the lowest elevation angle of 0.5°, the radar beam center over the Yogyakarta hail-report centroid was estimated at approximately 1.0 km above mean sea level, assuming standard atmospheric refraction with an effective Earth-radius factor of 4/3. Thus, radar reflectivity characterized storm intensity and hail-supporting convective morphology, while surface reports remained the primary evidence of hail reaching the ground. Because high reflectivity in humid tropical convection may result from heavy rainfall, graupel, hail, or mixed-phase hydrometeors, radar signatures were interpreted together with surface reports, satellite diagnostics, and environmental information.

A radar-based hail-likelihood classification was derived from composite maximum reflectivity. Grid cells with CMAX values of 45–50 dBZ were classified as possible hail-supporting signatures, 50–55 dBZ as probable hail-supporting signatures, and ≥55 dBZ as strong hail-supporting signatures. These thresholds were selected empirically through event-based calibration against the timing and spatial clustering of surface hail reports, after several candidate reflectivity ranges were inspected during the peak convective period. The classification was interpreted as a radar-based proxy for hail-supporting convection rather than as a deterministic hail-detection

algorithm; therefore, the thresholds should be regarded as case-specific diagnostic thresholds rather than universal hail-detection criteria.

To reduce pixel-scale noise and improve spatial coherence, isolated reflectivity features were filtered before object identification. Only coherent high-reflectivity regions were retained for comparison with reported hail locations and WRF-derived hail-supporting proxies. The resulting radar-based objects were used to evaluate whether intense convective cores developed near the hail-report cluster and coincided with the reported surface hail occurrence.

Because the hail-report region was located at relatively long range from the Semarang radar, radar sampling limitations were considered in the interpretation. Beam broadening, increasing beam height with range, and possible attenuation may affect the representation of storm-scale hydrometeor structures. Accordingly, composite maximum reflectivity was used to characterize vertically integrated convective-core intensity, while conclusions regarding surface hail occurrence were based on combined evidence from surface reports, radar-derived hail-likelihood signatures, satellite-observed convective deepening, and environmental diagnostics.

2.3 Himawari-9 satellite cloud-top diagnostics

Himawari-9 infrared observations were used to characterize cloud-top thermal evolution and rapid convective deepening associated with the hail-producing storm [65]–[70]. Because satellite infrared brightness temperature provides information on upper-cloud development rather than direct hail occurrence, the satellite analysis was used as complementary evidence to radar observations, surface hail reports, and environmental diagnostics. This approach helped determine whether surface-reaching hail occurred during rapid convective growth, mature storm development, or later cold-cloud expansion.

The primary satellite variable was infrared brightness temperature. Minimum cloud-top brightness temperature was calculated within the hail-report domain to identify the timing of the most intense convective growth, while cold cloud-top areas were computed using $BT \leq -50°C$, $BT \leq -60°C$, and $BT \leq -70°C$ thresholds. These thresholds distinguished deep, very deep, and extremely cold convective cloud regions associated with rapid vertical development [71]–[76].

Satellite-derived diagnostics were not interpreted as direct evidence of hail occurrence because cold cloud tops do not provide direct information on hail growth, hailstone size, melting during descent, or surface hailfall. Himawari-9 observations were therefore used as complementary evidence to assess whether the reported surface hail occurred during rapid convective deepening and intense upper-level cloud development.

The temporal evolution of minimum brightness temperature and cold cloud-top area was compared with the reported hail time and radar-derived hail-likelihood evolution. This comparison determined whether surface hail occurrence coincided with rapid cloud-top cooling, mature convective development, or later anvil expansion, since maximum cold-cloud shield extent may occur after the most intense hail-producing updraft phase. Satellite diagnostics were then interpreted together with radar observations and surface reports to reconstruct the life cycle of the hail-producing convective storm.

2.4 Environmental analysis

The pre-storm thermodynamic and kinematic environment was analyzed to assess whether atmospheric conditions supported deep convection and surface-reaching hail formation. Atmospheric sounding data closest to the hail-producing period were used to derive convective available potential energy, convective inhibition, lifting condensation level, freezing-level height, wet-bulb zero height, and vertical wind shear [77]–[82]. These parameters were used to evaluate instability, inhibition, low-level moisture, cloud-base height, storm organization potential, and the depth of the warm layer through which hailstones descended before reaching the surface.

Particular attention was given to freezing-level height and wet-bulb zero height because high freezing levels and deep warm layers increase hail melting potential in humid tropical environments. Under such conditions, surface-reaching hail requires sufficient instability, strong updrafts, efficient mixed-phase hydrometeor growth, and rapid downward transport through precipitation loading or downdraft processes.

Vertical wind shear was evaluated to determine whether the storm environment resembled a strongly organized mid-latitude severe-storm setting or a localized tropical severe-convection regime. Deep-layer shear was used to assess storm organization potential, while low-level to mid-level shear was used to infer convective structure and persistence. This distinction is important because tropical hail-producing storms may occur without classic supercell-like organization when localized instability release and mesoscale lifting produce intense short-lived updrafts.

To examine mesoscale lifting, ERA5 925-hPa wind and horizontal divergence fields were analyzed from 07:00 to 09:00 UTC, with negative divergence interpreted as low-level convergence. The analysis focused on whether convergence features were present near the Yogyakarta hail-report region before and during the reported hail occurrence. Low-level convergence was considered important because it can focus moisture, enhance upward motion, and support rapid convective intensification in a weakly to moderately sheared tropical atmosphere.

The environmental analysis was used as contextual physical evidence rather than as a deterministic hail predictor. Sounding-derived parameters and ERA5 low-level convergence fields were interpreted together with surface reports, radar-observed intensification, satellite cloud-top cooling, and WRF simulations to assess whether the storm developed within an environment favorable for intense tropical convection and hail survival to the surface.

2.5 WRF simulation and data assimilation experiments

Numerical simulations were conducted using the Weather Research and Forecasting model version 4.6.1 to examine the representation of the hail-producing convective storm under different data assimilation configurations [43], [77], [83]. The model used four one-way nested domains with horizontal grid spacing of 27 km, 9 km, 3 km, and 1 km, respectively. The innermost 1-km domain, with 40 vertical levels, was used as the primary analysis domain for storm-scale evaluation over the Yogyakarta hail-report region.

Initial and lateral boundary conditions were derived from the NCEP Global Forecast System 0.25° × 0.25° analysis initialized at 00:00 UTC on 11 March 2025. A 6-h spin-up period was applied before the main convective evaluation period to allow mesoscale thermodynamic adjustment, boundary-layer evolution, and hydrometeor-field development prior to the peak convective phase. The simulations were designed as event-scale storm-representation experiments rather than rapid-update nowcasting cycles. The physical parameterization schemes included WSM6 microphysics, RRTM longwave radiation, Dudhia shortwave radiation, the Yonsei University planetary boundary-layer scheme, and the Noah land surface model. No cumulus parameterization was used, allowing convection to be explicitly represented, particularly within the 3-km and 1-km domains.

Data assimilation was conducted using the three-dimensional variational data assimilation system of WRFDA at 00:00 UTC on 11 March 2025. The experiments were designed to evaluate the relative contribution of different observation types to simulated storm morphology, reflectivity intensity, and hail-supporting convective signatures. BMKG volumetric radar observations, including reflectivity and radial velocity depending on the experiment, were assimilated after retaining reflectivity values greater than 0 dBZ for quality control. Himawari-9 satellite observations from JAXA were assimilated to constrain cloud-field development, while NCEP ADP PREPBUFR conventional observations, including surface synoptic and upper-air observations, were used to adjust the initial atmospheric state.

Seven experiments were conducted to isolate the influence of different observational constraints. NODA served as the control simulation without data assimilation. DAIN assimilated conventional in-situ observations, DARFL assimilated radar reflectivity, DAV assimilated radar radial velocity, DARFLRV combined radar reflectivity and radial velocity, DAST assimilated Himawari-9 satellite observations, and DAALL assimilated all available observation types, including radar, satellite, surface synoptic, and upper-air observations. The experimental design and main constraints of each experiment are summarized in **Table 2**.

Table 2. Summary of WRFDA-3DVAR data assimilation experiments used to evaluate the representation of the hail-producing convective storm.

Experiment	Assimilated observations	Main constraint	Expected contribution
NODA	None	Baseline simulation	Control experiment without observational correction
DAIN	NCEP ADP PREPBUFR conventional observations, including surface synoptic and upper-air observations	Initial thermodynamic and kinematic state	Adjustment of the pre-convective atmospheric environment
DARFL	Radar reflectivity	Hydrometeor and precipitation structure	Improvement of simulated storm intensity, reflectivity morphology, and precipitation-core placement
DAV	Radar radial velocity	Storm-scale wind and kinematic structure	Improvement of storm dynamics, low-level flow organization, and convective placement
DARFLRV	Radar reflectivity and radial velocity	Hydrometeor field and storm kinematics	Joint correction of storm intensity and dynamical organization
DAST	Himawari-9 satellite observations	Cloud-field and cloud-top representation	Improvement of convective cloud development and spatial continuity

DAALL	Radar reflectivity, radar radial velocity, Himawari-9 satellite observations, surface synoptic observations, and upper-air observations	Multi-source atmospheric and storm-scale constraints	Integrated reconstruction of the storm environment and convective structure

These experiments were compared to determine how different observation types influenced the simulated hail-producing storm. Radar reflectivity assimilation was expected to affect hydrometeor loading and reflectivity morphology, radial-velocity assimilation to constrain storm-scale kinematics, satellite assimilation to improve broader cloud-field structure, and conventional observations to refine the pre-convective environment. The all-source experiment tested whether combining all available observations improved storm reconstruction or introduced structural overexpansion.

The simulated maximum column reflectivity and hydrometeor fields from each experiment were compared with radar-observed reflectivity and reported hail locations during the peak convective period. These outputs were then used to derive the synthetic reflectivity-based hail-supporting proxy described in Section 2.6 and to evaluate the sensitivity of tropical hail-supporting convection simulation to observation type and WRFDA-3DVAR configuration.

2.6 Synthetic Reflectivity-Based Hail Proxy Algorithm

A synthetic reflectivity-based hail-supporting proxy was developed to identify convective regions in the WRF simulations that were potentially favorable for hail production. This approach was applied because explicit radar reflectivity or hail-mixing-ratio variables were not available in the WRF output. Instead, the available model variables included rainwater mixing ratio, graupel mixing ratio, snow mixing ratio, perturbation pressure, base-state pressure, and perturbation potential temperature. The proxy was therefore designed to estimate hail-supporting convective signatures from hydrometeor loading and vertical reflectivity structure.

The total atmospheric pressure was calculated as the sum of perturbation pressure and base-state pressure:

$$P_{\text{tot}} = P + P_B$$

where P_{tot} is total pressure, P is perturbation pressure, and P_B is base-state pressure. Potential temperature was obtained by adding the WRF reference value of 300 K to the perturbation potential temperature:

$$\theta = T + 300$$

where θ is potential temperature and T is perturbation potential temperature. Air temperature was then estimated using the Poisson relationship:

$$T_k = \theta \left(\frac{P_{\text{tot}}}{P_0}\right)^{R_d/C_p}$$

where T_k is air temperature in Kelvin, P_0=100000 Pa is the reference pressure, R_d=287.05 J kg^{-1} K^{-1} is the gas constant for dry air, and C_p =1004 J kg^{-1} K^{-1} is the specific heat of dry air at constant pressure.

Air density was calculated using the ideal gas equation:

$$\rho = \frac{P_{\text{tot}}}{R_d T_k}$$

where ρ is air density. The hydrometeor mixing ratios were then converted into mass concentrations or water contents:

$$WC_i = \rho q_i$$

where WC_i is the water content of hydrometeor species i, and qi represents the mixing ratio of rainwater (qr), graupel (qg), or snow (qs).

Synthetic linear reflectivity was estimated from rainwater, graupel, and snow water contents using an empirical weighted formulation:

$$Z_l in = \alpha_r WC_r^{\beta} + \alpha_g WC_g^{\beta} + \alpha_s WC_s^{\beta}$$

where Z_{lin} is the synthetic linear reflectivity, WC_r, WC_g, and WC_s are the water contents of rainwater, graupel, and snow, respectively. The coefficients α_r, α_g, and α_s are empirical weighting factors, while β is an empirical exponent controlling the nonlinear sensitivity of reflectivity to hydrometeor concentration. Graupel was assigned a larger relative weight than rainwater and snow because it is more directly associated with intense mixed-phase microphysical processes and hail-supporting convection.

The synthetic reflectivity factor was converted into logarithmic reflectivity units as follows:

$$Z_{\text{dBZ}} = 10 \log_{10}(Z_{lin} + \epsilon)$$

where Z_{dBZ} is synthetic reflectivity in dBZ and ϵ is a small positive constant introduced to avoid undefined logarithmic values when hydrometeor concentrations approach zero.

Since synthetic reflectivity was calculated at each model level, a composite synthetic reflectivity field was obtained by taking the vertical maximum:

$$Z_{\text{comp}}(x, y) = \max_z [\text{dBZ}(z, x, y)]$$

where $Z_{comp}(x, y)$ represents the maximum synthetic reflectivity within the atmospheric column at each horizontal grid point.
The hail-supporting proxy was then classified using composite synthetic reflectivity thresholds:

$$H(x,y) = \begin{cases} 0, & Z_{comp} < 45\ dBZ \\ 1, & 45 \le Z_{comp} < 50\ dBZ \\ 2, & 50 \le Z_{comp} < 55\ dBZ \\ 3, & Z_{comp} \ge 55\ dBZ \end{cases}$$

where H(x,y) represents the hail-supporting proxy class. A value of 0 indicates no hail-supporting signal, 1 indicates possible hail-supporting convection, 2 indicates probable hail-supporting convection, and 3 indicates strong hail-supporting convection.

The composite synthetic reflectivity field was smoothed using a Gaussian filter before classification to reduce grid-scale noise and improve object coherence. Binary opening and closing were applied to remove isolated features and fill minor gaps, while dilation slightly expanded coherent hail-supporting regions to account for small displacement uncertainty between simulated and observed storm objects. Class overlap was avoided by assigning categories sequentially from the highest-intensity class to probable and possible hail-supporting classes. The resulting proxy was interpreted as an indicator of hail-supporting convective conditions rather than a direct prediction of surface-reaching hail, which is also controlled by hailstone size distribution, growth and melting history, fall trajectory, downdraft strength, and near-surface thermodynamics. Accordingly, the proxy was used mainly for relative comparison among WRF data assimilation experiments and for spatial consistency assessment against radar-derived hail-likelihood fields and surface hail reports.

2.7 Verification metrics

The representation of the hail-producing convective storm was evaluated using categorical, object-based, and scale-aware spatial verification metrics, because hail-supporting convective cores are compact, short-lived, and sensitive to small displacement errors. Categorical verification was first used to compare radar-derived hail-likelihood areas with WRF-derived hail-supporting proxy fields. Hits, misses, false alarms, and correct negatives were defined from a contingency table [84], from which probability of detection, false alarm ratio, critical success index, frequency bias, and proportion correct were calculated to assess direct spatial correspondence between observed and simulated hail-supporting areas. However, these grid-point scores were interpreted cautiously because they may penalize physically meaningful convective cores displaced by only a few kilometers, while overly broad hail-supporting areas may still obtain high hit rates despite unrealistic storm structure. Therefore, categorical scores were used as supplementary diagnostics rather than the sole basis for assessing representation improvement.

Object-based verification was used as the primary framework for evaluating storm-scale representation. The structure–amplitude–location (SAL) metric was applied to quantify differences between radar-observed and WRF-simulated convective objects[85], [86]. Its structure component represents differences in object morphology and spatial distribution, the amplitude component represents reflectivity-intensity differences, and the location component represents displacement between observed and simulated objects; lower SAL values indicate better agreement. Additional spatial metrics complemented SAL, including centroid distance error, hit rate, intersection-over-union, and fractions skill score, which respectively measured object displacement, captured observed area, spatial overlap, and scale-aware agreement while reducing excessive penalties from small displacement errors.

Together, these metrics distinguished different aspects of model performance. A simulation with low distance error and low SAL was interpreted as having better storm-object realism, whereas high hit rate with poor SAL suggested potentially overexpanded hail-supporting areas. This distinction is important for tropical surface-reaching hail, which depends on localized intense convection rather than broad convective coverage. Therefore, representation improvement was assessed through the combined interpretation of storm structure, intensity, displacement, overlap, and scale-aware spatial agreement.

The overall workflow of the multi-source data assimilation and hail-supporting convection representation analysis is summarized in **Figure 2**. The framework integrates surface hail reports, radar observations, Himawari-9 satellite data, environmental diagnostics, WRFDA-3DVAR experiments, synthetic reflectivity-based hail-supporting proxy generation, and multi-metric verification. This design enables the evaluation of whether different assimilation strategies improve the representation of hail-supporting tropical convection in terms of both physical realism and spatial predictability.

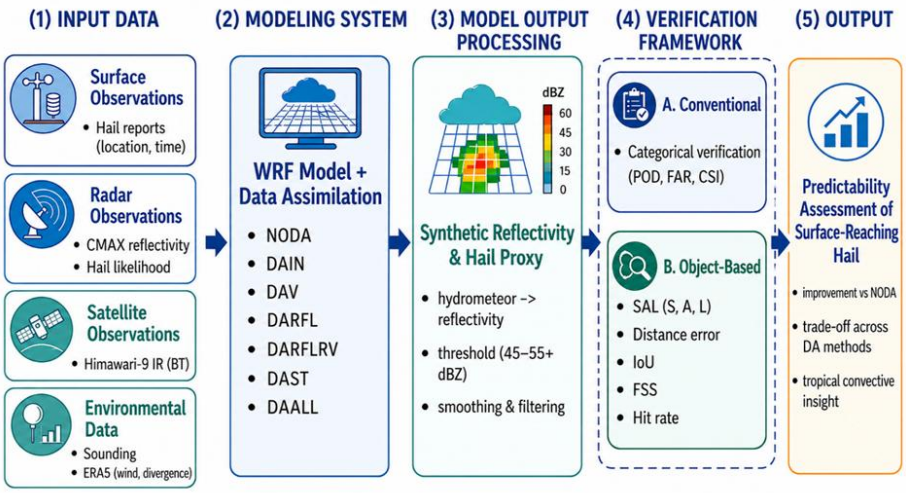


Figure 2. Conceptual framework for evaluating hail-supporting tropical convection using surface reports, radar observations, Himawari-9 satellite data, environmental diagnostics, WRFDA-3DVAR experiments, synthetic reflectivity-based hail proxies, and multi-metric verification.

3. Results

3.1 Observed evolution of the surface-reaching hail event

Surface-reaching hail was reported over the Yogyakarta region at approximately 08:15 UTC on 11 March 2025. After duplicate and closely overlapping records were removed, 11 unique hail-report locations were retained for event reconstruction and verification. These reports were concentrated along the Sleman–Yogyakarta urban corridor, with additional reports extending toward parts of Bantul. As shown in **Figure 1** and summarized in **Table 1**, the reported locations formed a compact spatial cluster rather than isolated point occurrences, indicating that the event was associated with a localized but coherent hail-producing convective system.

The retained hail-report locations included Mlati, Depok, Gamping, Ngaglik, Tajem, Jalan Kaliurang, Jalan Magelang, the UGM campus area, Tegalrejo, Kasihan, and the Ringroad Barat corridor. This distribution indicates that the main hail-affected zone was located over the northern to central part of the Yogyakarta urban region, particularly within the Sleman–Yogyakarta corridor. The clustering of reports provides an observational anchor for evaluating whether radar-derived hail-likelihood signatures and WRF-derived hail-supporting proxy fields captured the approximate spatial footprint of the storm.

Reported hailstones were described as ranging from small gravel-like particles to larger pellets comparable to coin-sized or rubber-bullet-sized fragments. Although instrumental hail-size measurements were unavailable, these qualitative reports provide direct evidence that frozen hydrometeors survived descent to the surface. In the humid tropical environment of Yogyakarta, where melting potential is high, surface-reaching hail implies that the parent convective storm developed sufficiently intense mixed-phase microphysics and rapid downward transport.

Reports of fallen trees and localized wind-related impacts were interpreted only as contextual evidence of severe convective conditions, not as independent verification of hail occurrence. Therefore, surface hail reports were used as the primary evidence of hail reaching the ground, whereas radar, satellite, environmental, and WRF-based diagnostics were used to reconstruct the storm evolution and evaluate the representation of hail-supporting convection.

3.2 Radar-observed storm intensification and hail-likelihood evolution

Radar observations showed rapid convective intensification over the Yogyakarta region between 07:20 and 08:40 UTC. During the early stage at 07:20–07:30 UTC, the strongest reflectivity cores were still located north of the main hail-report cluster, indicating that the convective system had not yet reached its peak intensity over the affected area. By 07:40–07:50 UTC, the convective core intensified and shifted closer to the Sleman–Yogyakarta corridor, marking the onset of rapid storm intensification (**Figure 3**).

The strongest radar reflectivity signatures occurred between 08:00 and 08:20 UTC, closely bracketing the reported hail occurrence at approximately 08:15 UTC. During this period, high-reflectivity cores became spatially aligned with several reported hail locations (**Figure 3**). Native-grid radar reflectivity reached a maximum value of approximately 67 dBZ near the hail-producing phase, indicating a highly intense convective core. The temporal and spatial correspondence between the radar maximum and surface reports suggests that the reported hail occurred during the mature stage of a rapidly intensifying storm cell.

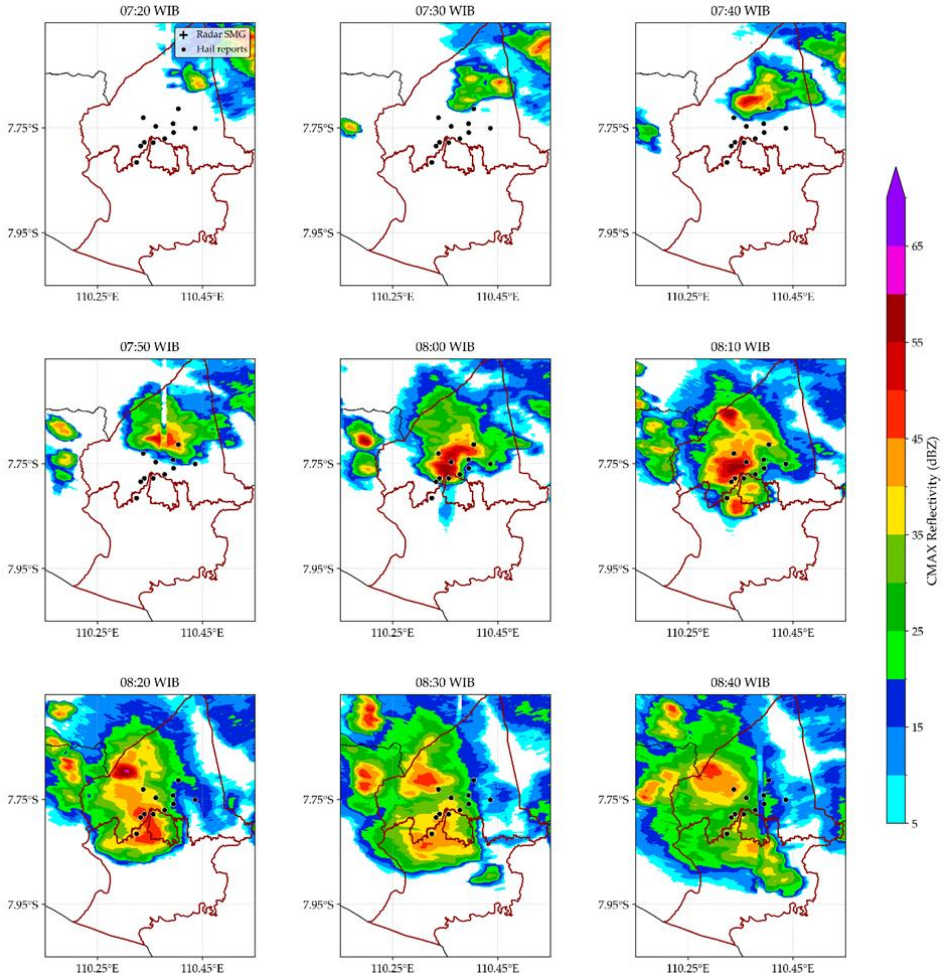


Figure 3. Temporal evolution of CMAX radar reflectivity over Sleman, Bantul, and Yogyakarta City during the hail-producing convective event on 11 March 2025 from 07:20 to 08:40 UTC. Panels show 10-min intervals, and black dots indicate reported surface hail locations. The convective system intensified rapidly after 07:40 UTC, with the strongest reflectivity occurring between 08:00 and 08:20 UTC, closely bracketing the reported hail occurrence at approximately 08:15 UTC.

The radar-based hail-likelihood classification further confirmed the short-lived nature of the hail-supporting phase. Possible hail-supporting signatures began to appear around 07:40 UTC and expanded rapidly after 07:50 UTC. Probable hail-supporting areas became more prominent near 08:00–08:10 UTC, whereas strong hail-supporting signatures were mainly confined to the 08:00–08:20 UTC interval (**Figure 4**). This pattern indicates that the hail-producing phase was brief, localized, and closely tied to the period of maximum convective intensity.

The temporal evolution of hail-likelihood area showed a clear peak around the reported hail time. The possible-hail category reached its maximum near 08:20 UTC, whereas the probable-hail category peaked earlier, around 08:10 UTC. Strong hail-supporting signatures appeared only during the peak convective window, suggesting that surface-reaching hail was linked to a short period of enhanced hydrometeor loading and intense mixed-phase convection (**Figure 5**). After 08:20 UTC, the hail-likelihood areas decreased and became more fragmented, indicating weakening of the hail-supporting core or displacement away from the main report cluster.

Overall, the radar evidence indicates that the Yogyakarta hail event was associated with a rapidly intensifying convective core whose strongest reflectivity and hail-likelihood signatures occurred within approximately 10–20 min of the reported surface hail time. This close temporal correspondence supports the use of the 08:00–08:20 UTC period as the key window for evaluating WRF-simulated storm structure and hail-supporting proxy fields.

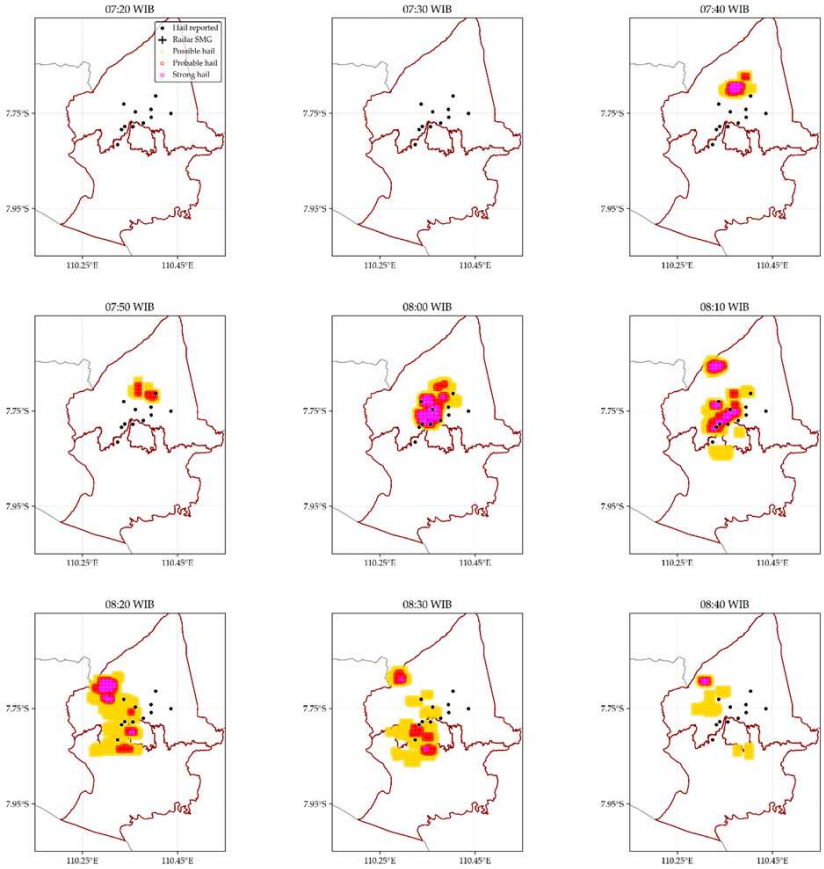


Figure 4. Spatial distribution of radar-based hail-likelihood categories over Yogyakarta from 07:20 to 08:40 UTC on 11 March 2025. The categories represent possible, probable, and strong hail-supporting signatures, while black dots indicate reported surface hail locations. The development and movement of hail-supporting signatures show increasing spatial alignment with the reported hail cluster during the peak convective phase.

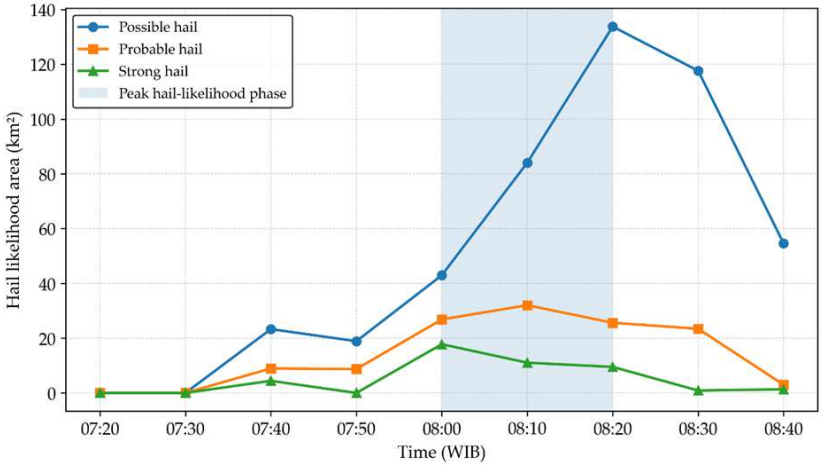


Figure 5. Time series of radar-based hail-likelihood area for possible, probable, and strong hail categories during the 11 March 2025 Yogyakarta hail event. The shaded interval indicates the peak hail-likelihood phase, and the dashed line marks the reported hail time at approximately 08:15 UTC.

3.3 Satellite-observed rapid convective deepening

Himawari-9 infrared observations showed rapid cloud-top cooling over the Yogyakarta region before and during the surface hail occurrence. During the early stage at 07:20–07:40 UTC, the coldest cloud tops were located north of the hail-report cluster, while the Yogyakarta region was still dominated by relatively warmer cloud-top temperatures (Figure 6). This indicates that the convective system had not yet reached its maximum vertical development over the affected area.

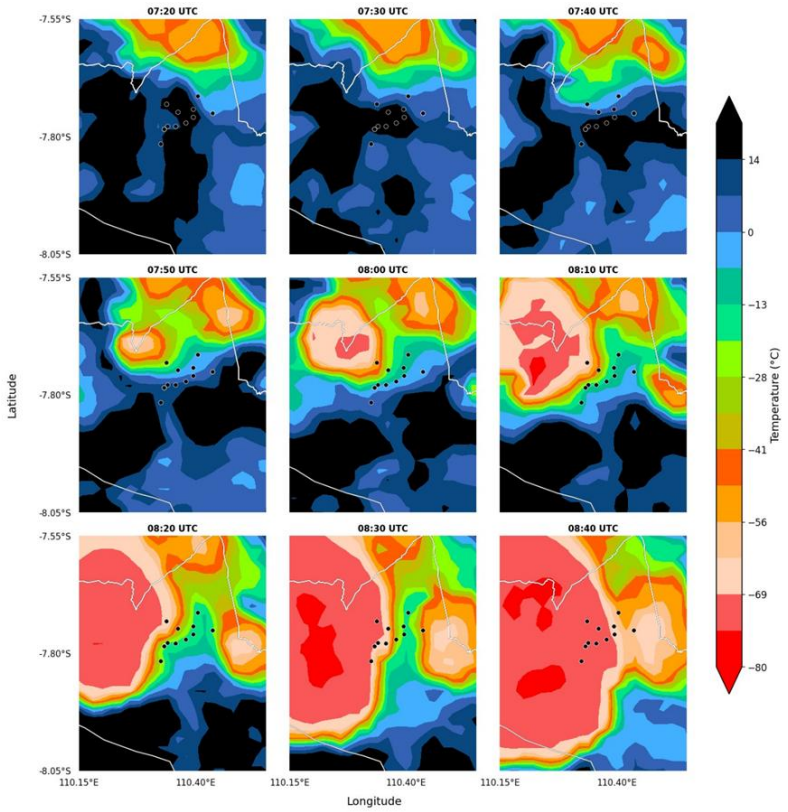


Figure 6. Himawari-9 infrared brightness temperature over Yogyakarta from 07:20 to 08:40 UTC on 11 March 2025. Black dots indicate reported surface hail locations. The progressive cooling and expansion of cold cloud-top regions indicate rapid convective development before and during the surface hail occurrence. The strongest spatial alignment between cold cloud tops and reported hail locations occurred around 08:10–08:20 UTC.

A pronounced convective-deepening phase occurred between 07:40 and 08:10 UTC. During this period, the minimum cloud-top brightness temperature decreased from approximately −53°C at 07:40 UTC to about −72°C at 08:00 UTC (**Figure 7**). This rapid cooling of nearly 20°C within 20 min indicates strong vertical cloud growth and intensifying deep convection. At the same time, the spatial extent of very cold cloud tops increased substantially. The area with brightness temperature ≤ −60°C expanded from near-zero values to more than 200 km², while regions with brightness temperature ≤ −70°C began to emerge during the same interval (**Figure 7**).

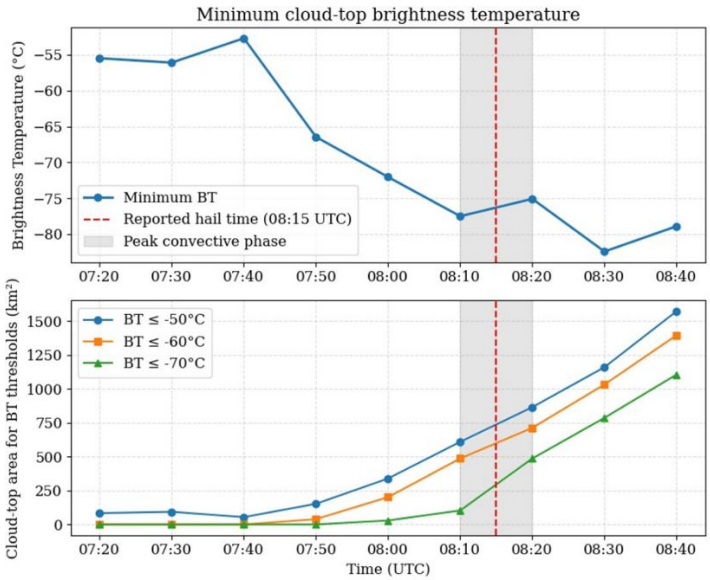


Figure 7. Time series of Himawari-9 infrared brightness temperature diagnostics over the hail-report domain on 11 March 2025. The upper panel shows minimum cloud-top brightness temperature, and the lower panel shows cold cloud-top areas for BT ≤ −50°C, BT ≤ −60°C, and BT ≤ −70°C. The dashed line marks the reported hail time at approximately 08:15 UTC, and the shaded interval denotes the peak convective phase.

The strongest alignment between cold cloud-top regions and the hail-report cluster occurred during 08:10–08:20 UTC, closely coinciding with the reported hail occurrence at approximately 08:15 UTC (Figure 6). This temporal correspondence indicates that hail occurred during the rapid convective-deepening phase rather than after the cold cloud shield reached its maximum spatial extent.

Importantly, the maximum spatial extent of cold cloud tops occurred slightly after the peak hail-producing phase. Although the area of brightness temperature ≤ −50°C continued to expand beyond 08:20 UTC, the most intense hail-supporting phase was associated with the earlier rapid cooling and development of very cold cloud cores, particularly those with brightness temperatures ≤ −60°C and ≤ −70°C (**Figure 7**). This suggests that surface-reaching hail was linked to the intensifying updraft phase rather than to the later mature anvil-expansion stage.

Overall, the satellite evidence indicates that the Yogyakarta hail event was associated with a short-lived but intense convective-deepening phase, characterized by rapid cloud-top cooling and expansion of very cold cloud regions within approximately 20–30 min before the reported hail occurrence. This behavior is consistent with strong vertical development and enhanced mixed-phase microphysical processes required to support hail formation in a humid tropical environment.

3.4 Pre-storm environment supporting tropical hail formation

The pre-storm sounding indicated that the Yogyakarta region was characterized by a moderately to strongly unstable tropical atmosphere before the hail event. Convective available potential energy reached approximately 1866 J kg^{-1}, while convective inhibition was weak, approximately −28 J kg^{-1} (**Figure 8**). This combination indicates that the atmosphere contained sufficient buoyant energy for deep convection and that only modest lifting was required to initiate or intensify convective development.

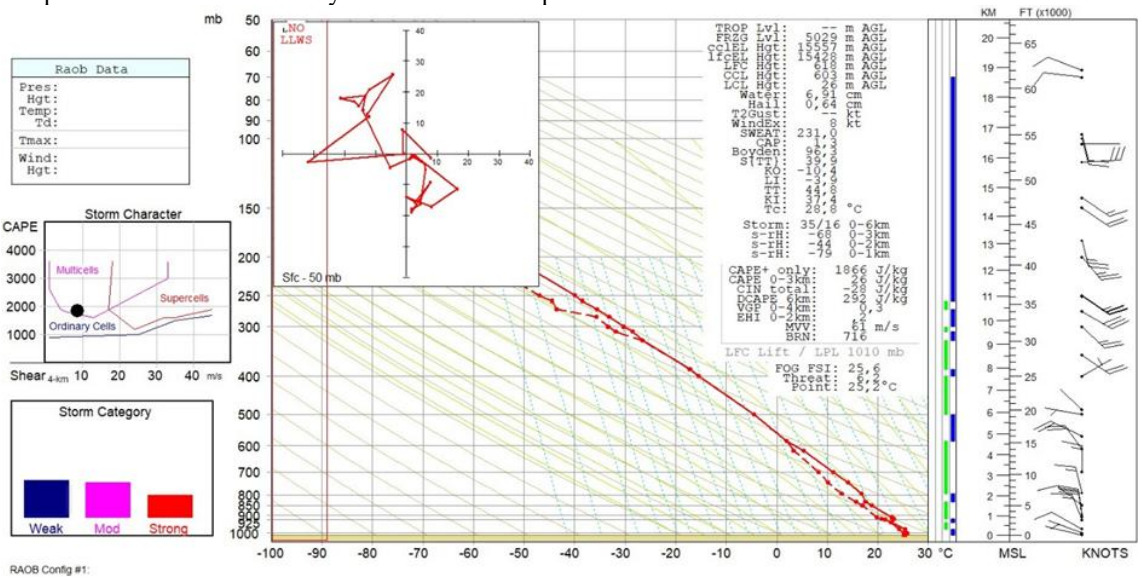


Figure 8. Pre-storm atmospheric sounding and hodograph near the hail-producing convective environment on 11 March 2025. The profile shows moderate-to-strong convective instability, with CAPE of approximately 1866 J kg^{-1}, weak CIN of around −28 J kg^{-1}, a low lifting condensation level near 616 m AGL, and a freezing level near 5029 m AGL. The wind profile indicates weak-to-moderate deep-layer shear, suggesting that hail production was likely associated with intense localized updrafts and mesoscale lifting rather than a strongly sheared supercell environment.

The lower troposphere was moist, with a lifting condensation level of approximately 616 m above ground level (**Figure 8**). This low cloud-base height indicates abundant low-level moisture and efficient parcel lifting into saturation. In a tropical convective environment, such a moist boundary layer can support rapid cloud growth once mesoscale convergence or local lifting mechanisms are present.

The freezing level was located near 5029 m above ground level, while the wet-bulb zero height reached approximately 6.91 km (**Figure 8**). These values indicate a deep warm layer beneath the melting level, which would normally favor substantial melting of falling ice particles before they reach the surface. Therefore, the occurrence of surface-reaching hail under these conditions implies that the parent storm developed sufficiently strong updrafts, efficient mixed-phase hydrometeor growth, and rapid downward transport to allow hailstones to survive descent through the warm tropical layer.

The kinematic environment was characterized by weak-to-moderate vertical wind shear. The 0–6 km shear was approximately 16 m s^{-1}, while the 0–3 km shear was approximately 8 m s^{-1} (**Figure 8**). These values suggest that the storm was not embedded within a classic strongly sheared supercell environment. Instead, the event was more consistent with a tropical severe-convection pathway, in which localized instability release and mesoscale lifting can produce short-lived but intense convective cores.

ERA5 925 hPa wind and horizontal divergence fields showed organized low-level convergence near southern Central Java and the Yogyakarta region before and during the hail-producing period. A convergence zone was already present near the event region at 07:00 UTC and became more organized around 08:00 UTC, close to the reported hail time (**Figure 9**). This convergence likely provided mesoscale lifting that helped release instability and intensify the convective storm over the hail-report region.

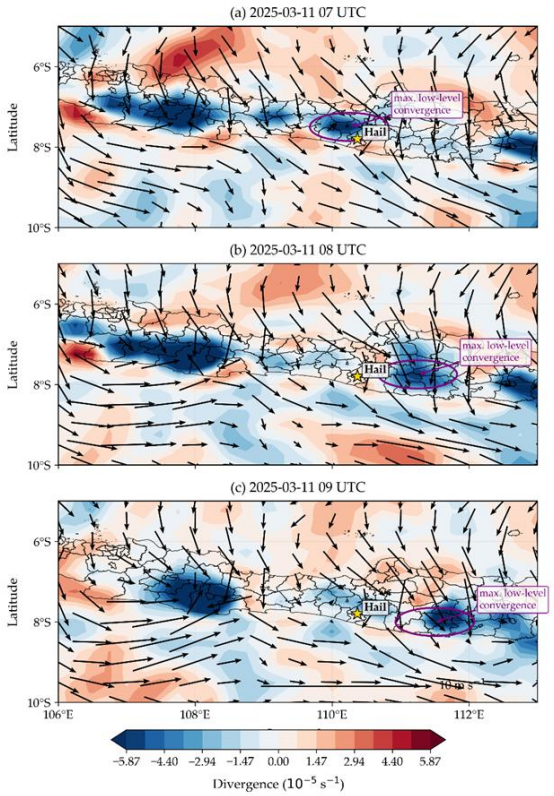


Figure 9. ERA5 925 hPa wind vectors and horizontal divergence over central–southern Java at (a) 07:00 UTC, (b) 08:00 UTC, and (c) 09:00 UTC on 11 March 2025. Shaded values represent divergence, with negative values indicating low-level convergence. The yellow star marks the centroid of reported hail occurrences over Yogyakarta, while purple ellipses indicate the maximum low-level convergence zone near the event region. The convergence maximum near Yogyakarta around 08:00 UTC indicates mesoscale lifting that supported rapid convective intensification before and during the reported hail occurrence.

Overall, the environmental analysis indicates that the hail-producing storm developed under a physically favorable but non-classical tropical severe-convection environment. The combination of moderate-to-strong instability, weak inhibition, abundant low-level moisture, high freezing level, weak-to-moderate shear, and organized low-level convergence suggests that surface-reaching hail was enabled by intense localized updraft development rather than classic supercell-scale storm organization.

3.5 Temporal evolution of simulated convective intensity

After the observed storm evolution and pre-storm environment were established, the temporal evolution of maximum reflectivity was examined to assess whether the WRF simulations reproduced the timing and magnitude of convective intensification. On the native radar grid, the observed storm showed a pronounced increase in maximum reflectivity from 04:00 to 08:00 UTC, reaching a peak value of approximately 67 dBZ near the reported hail-producing period (**Figure 10**). This indicates that the surface hail event occurred during the maximum-intensity phase of the convective system.

The WRF simulations generally reproduced the timing of convective intensification, with most experiments showing peak reflectivity between 07:00 and 08:00 UTC (**Figure 10**). This temporal agreement suggests that the model captured the broad timing of storm development and intensification. However, the simulated peak reflectivity values were generally lower than the native-grid radar maximum, with most WRF experiments producing maximum reflectivity values in the range of approximately 55–60 dBZ. This indicates that the simulations underestimated the most extreme convective-core intensity associated with the observed hail-producing storm.

The difference between the native radar maximum reflectivity in **Figure 10** and the radar maximum reflectivity used in the verification table should be interpreted in terms of processing stage. **Figure 10** shows the radar maximum reflectivity on the native radar grid before regridding, preserving local pixel-scale reflectivity

extrema. In contrast, the radar maximum reflectivity reported in the object-based verification was calculated after interpolation onto the 1-km WRF verification grid and extraction within the verification object. This regridding and object-masking procedure reduces local extrema and yields a lower radar maximum reflectivity value than the native-grid peak. Therefore, the difference reflects spatial harmonization required for fair radar–WRF comparison rather than an inconsistency in the radar dataset.

Overall, the temporal analysis shows that WRF reproduced the general timing of convective intensification but underestimated the observed native-grid peak reflectivity. This result supports the use of WRF simulations for evaluating relative differences among data assimilation experiments, while also highlighting limitations in representing the most extreme storm-core intensity associated with surface-reaching hail.

Having assessed the temporal behavior of the simulations, the next section evaluates how different data assimilation configurations affected the spatial structure and morphology of the simulated storm.

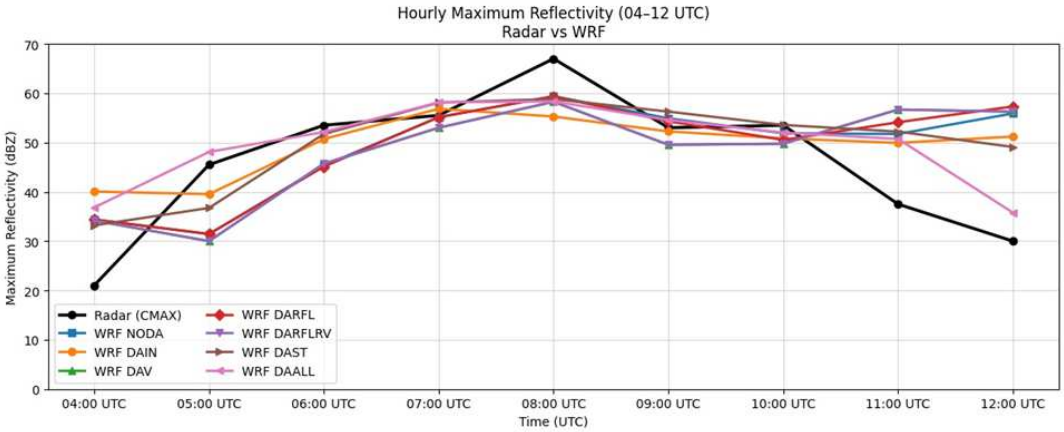


Figure 10. Temporal evolution of hourly maximum reflectivity from radar observations and WRF simulations during the convective event from 04:00 to 12:00 UTC on 11 March 2025. Radar observations and WRF simulations are compared to assess the timing and magnitude of convective intensification.

3.6 Impact of data assimilation on simulated storm reconstruction

WRF simulations showed substantial sensitivity to the assimilated observation type in representing the hail-producing convective storm. Compared with the radar-observed convective core, the NODA experiment reproduced convective activity over the broader Yogyakarta region but showed clear displacement and fragmentation of the simulated reflectivity structure (**Figure 11**). This indicates that the control simulation was able to generate deep convection, but failed to accurately reproduce the observed storm placement and coherent convective morphology during the hail-producing period.

Assimilation experiments modified the simulated storm structure in distinct ways. DARFL produced a stronger and more spatially coherent reflectivity core closer to the observed radar object, indicating that radar reflectivity assimilation directly improved the simulated hydrometeor and precipitation structure (**Figure 11**). This result is physically consistent with the role of reflectivity assimilation in constraining precipitation-sized hydrometeors and convective-core intensity.

DAV improved aspects of storm-scale organization but produced a more limited improvement in reflectivity structure compared with DARFL (**Figure 11**). This suggests that radial-velocity assimilation helped constrain the kinematic field, but its effect on hydrometeor loading and reflectivity morphology was indirect. DARFLRV, which combined reflectivity and radial-velocity assimilation, produced a storm structure that partly reflected both microphysical and kinematic constraints, although the improvement was not uniformly superior to DARFL alone.

DAST showed a different response by improving broader cloud-field continuity and convective coverage, but it did not provide the same direct constraint on the near-storm precipitation core as radar reflectivity assimilation (**Figure 11**). DAIN primarily adjusted the initial thermodynamic and kinematic environment and showed limited direct correction of the convective reflectivity object during the peak hail-producing period. These results indicate that observation types that directly constrain storm-scale precipitation structures are more effective for reproducing compact hail-supporting convective cores than observations that primarily constrain the broader environment or cloud shield.

The DAALL experiment produced the broadest simulated convective coverage among the assimilation experiments (**Figure 11**). Although this configuration incorporated all available observations, the resulting reflectivity field appeared spatially overexpanded relative to the observed radar object. This indicates that multi-source assimilation did not automatically yield the most realistic convective-scale reconstruction. Instead, the combined observational constraints may have increased storm coverage while degrading object compactness and structural realism.

Visually, DARFL provided the most coherent reconstruction of the observed convective core, especially in terms of placement and reflectivity morphology. This qualitative pattern is evaluated quantitatively in Section 3.8 using object-based metrics that assess storm morphology, amplitude, displacement, and spatial overlap across all experiments.

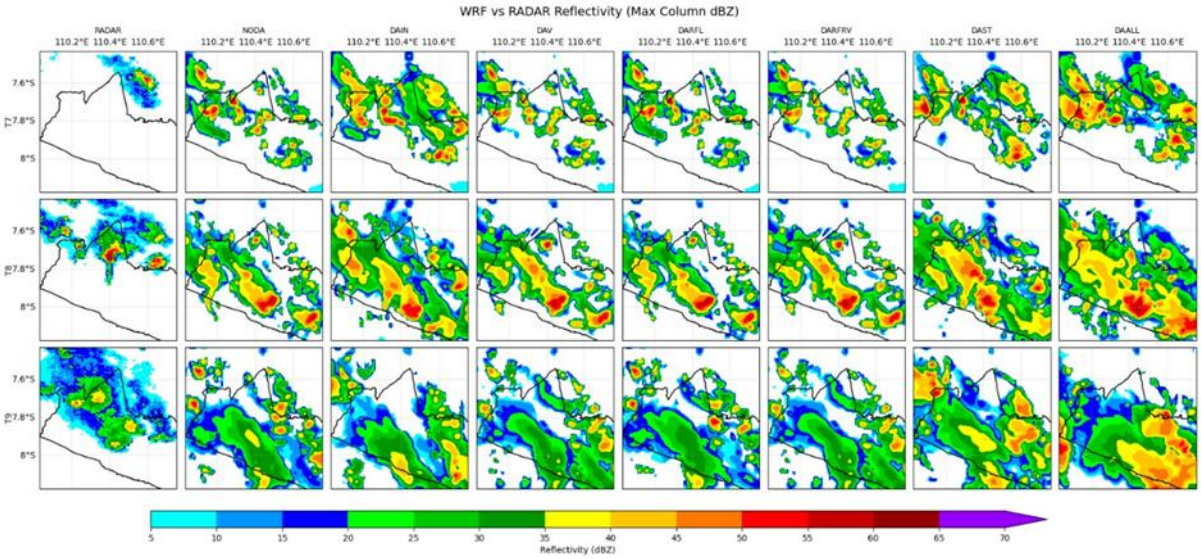


Figure 11. Comparison between observed radar reflectivity and WRF-simulated maximum column reflectivity for different data assimilation experiments during the hail event on 11 March 2025. The first column shows radar observations, while subsequent columns show simulations from NODA, DAIN, DAV, DARFL, DARFLRV, DAST, and DAALL. Rows represent successive time steps during the convective evolution.

3.7 Representation of surface-reaching hail in WRF simulations

The synthetic reflectivity-based hail-supporting proxy was used to evaluate whether each WRF experiment reproduced convective regions consistent with the observed hail-producing storm. The radar-derived hail-likelihood field at 08:00 UTC showed compact possible, probable, and strong hail-supporting signatures near the reported hail cluster (**Figure 12**). This pattern indicates that the observed hail-producing phase was spatially localized and associated with a compact high-reflectivity convective core rather than widespread convective coverage.

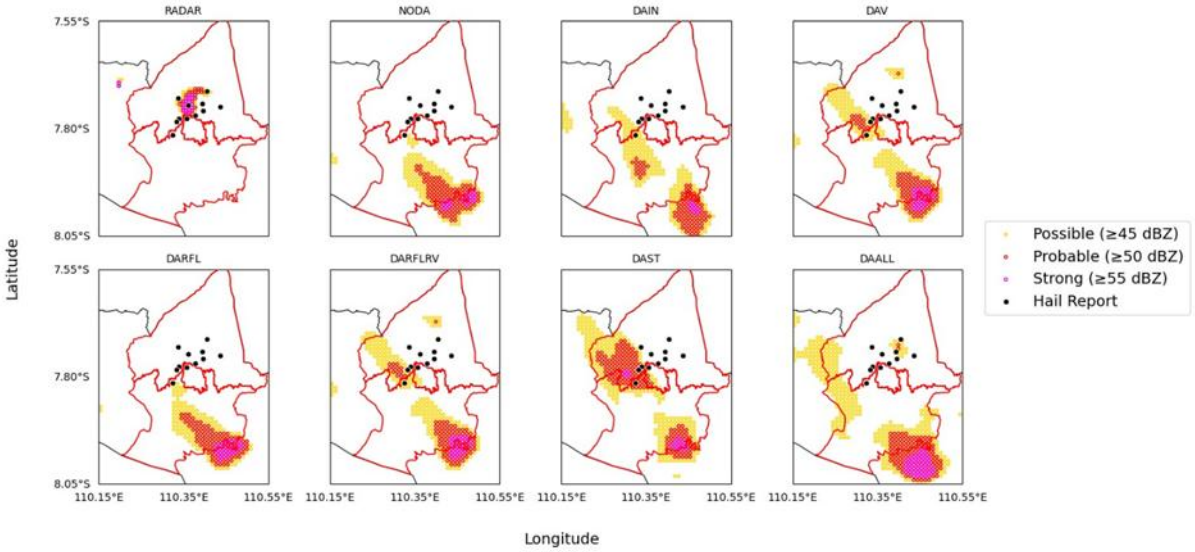


Figure 12. Spatial comparison of radar-derived hail likelihood and WRF-derived hail-proxy footprints at 08:00 UTC for different data assimilation experiments. The radar panel shows radar-based hail likelihood, while the WRF panels show synthetic reflectivity-based hail-proxy categories for NODA, DAIN, DAV, DARFL, DARFLRV, DAST, and DAALL. Yellow, red, and magenta markers indicate possible, probable, and strong hail categories, respectively. Black dots represent reported surface hail locations, and the plus symbol denotes the Semarang radar. Radar reflectivity is shown on the native radar grid before regridding to the WRF verification grid.

The NODA experiment produced a hail-supporting proxy signal, but the main proxy footprint was displaced from the reported hail locations (**Figure 12**). This indicates that the control simulation was able to generate intense convection with hail-supporting characteristics, but failed to reproduce the observed spatial placement of the hail-producing core. This displacement is important because even small location errors can strongly affect the diagnosis of localized surface-reaching hail.

Among the assimilation experiments, DARFL produced one of the most spatially consistent hail-supporting proxy patterns relative to the radar-derived hail-likelihood field and surface hail reports (**Figure 12**). The proxy region in DARFL was more coherent and better aligned with the observed hail-report corridor than in NODA, suggesting that radar reflectivity assimilation improved the representation of hydrometeor loading and storm-core placement. This result is consistent with the improvement in storm reflectivity morphology described in Section 3.6.

DAV and DARFLRV showed more limited improvement in the hail-supporting proxy footprint. Although radial-velocity assimilation can constrain storm-scale kinematics, its indirect influence on hydrometeor loading may explain why the resulting hail-proxy areas were less consistently aligned with the observed hail-supporting region (**Figure 12**). DAST and DAIN produced broader or less spatially focused hail-supporting signals, indicating that cloud-field or environmental adjustments alone were insufficient to reproduce the compact hail-producing core.

DAALL generated the broadest hail-supporting proxy footprint among the experiments. Although this increased overlap with parts of the hail-report region, the simulated area was substantially broader than the radar-derived hail-likelihood object, indicating a tendency toward spatial overexpansion.

Overall, the hail-supporting proxy analysis indicates that radar reflectivity assimilation improved the spatial consistency of simulated hail-supporting convection relative to the observed storm. However, the results also show that broader proxy coverage does not necessarily represent better hail-related storm representation. The proxy should therefore be interpreted together with object-based verification metrics to distinguish genuine improvement in storm-core placement and morphology from overexpanded simulated convection.

3.8 Object-Based Verification of Storm-Representation Gains

Object-based verification was used to quantify how different data assimilation configurations affected the representation of the hail-producing convective storm. The verification was conducted using radar-observed reflectivity and WRF-simulated maximum column reflectivity at 08:00 UTC, corresponding to the peak hail-producing period. The results are summarized in **Table 3**. Lower values of structure–amplitude–location and distance error indicate better agreement with the radar-observed storm object, whereas higher values of hit rate, intersection-over-union, and fractions skill score indicate better spatial correspondence.

Table 3. Object-based verification of WRF-simulated hail-producing convection against radar-observed reflectivity at 08:00 UTC. S, A, and L represent the structure, amplitude, and location components of SAL. Distance error measures object displacement, while hit rate, intersection-over-union, and fractions skill score quantify spatial agreement. Radar Max dBZ refers to the regridded and object-masked radar reflectivity used for verification.

Experiment	S	A	L	Total SAL	Distance Error	Hit Rate	IoU	FSS	WRF Max dBZ	Radar Max dBZ	Main Interpretation
NODA	0.9	0.8	0.1	1.3	1.8	0.8	0.1	0.2	59.4	52.2	Baseline
DAIN	1.3	1.2	0.1	1.8	4.4	0.7	0.1	0.2	55.3	52.2	Degraded structure and overlap
DAV	1.1	0.9	0.1	1.4	3.9	0.6	0.1	0.2	58.3	52.2	Limited improvement
DARFL	0.9	0.8	0.1	1.2	1.8	0.7	0.1	0.2	59.3	52.2	Best SAL and distance agreement
DARFLRV	1.1	0.9	0.1	1.4	3.9	0.6	0.1	0.2	58.3	52.2	Similar to DAV
DAST	1.3	1.3	0.1	1.8	3.9	0.8	0.1	0.2	58.8	52.2	Higher hit rate but weaker structure
DAALL	1.4	1.4	0.0	2.0	2.6	1.0	0.1	0.2	58.3	52.2	Highest hit rate but overexpanded structure

The NODA experiment produced a total SAL value of 1.272 and a distance error of 1.835, indicating moderate disagreement in storm-object structure and placement relative to the radar observation. This confirms that the control simulation generated deep convection near the study region, but still contained displacement and structural errors. The hit rate of 0.754 suggests that part of the observed convective area was captured, although the low intersection-over-union value of 0.112 indicates limited spatial overlap between observed and simulated objects.

Among all experiments, DARFL produced the best overall object-based agreement, with the lowest total SAL value of 1.235 and the lowest distance error of 1.768 (**Table 3**). Its structure component was also lower than that of NODA, indicating improved storm-object morphology. This result supports the interpretation that radar reflectivity assimilation most effectively improved the placement and structural realism of the simulated hail-producing convective core.

DAIN, DAV, and DARFLRV showed weaker verification performance than DARFL. DAIN produced a higher total SAL value of 1.764 and a larger distance error of 4.388, indicating degraded storm-object agreement after assimilation of conventional observations alone. DAV and DARFLRV produced similar total SAL values of 1.372 and distance errors of 3.935, suggesting that radial-velocity assimilation improved neither storm placement nor reflectivity-object morphology as effectively as reflectivity assimilation in this case.

DAST and DAALL produced relatively high hit rates but poorer structural performance. DAST achieved a hit rate of 0.835, while DAALL produced the highest hit rate of 0.991. However, these high hit rates were accompanied by larger total SAL values of 1.833 and 1.976, respectively (**Table 3**). This indicates that both experiments captured a larger fraction of the observed convective area, but did so by producing broader or structurally distorted simulated storm objects. In particular, DAALL achieved the highest areal coverage but the poorest overall SAL performance, suggesting overexpanded convection.

The fractions skill score showed only modest variation among experiments, with values ranging from 0.164 in DAIN to 0.232 in NODA and 0.231 in DARFL. This indicates that, at the verification scale used, DARFL nearly matched the best scale-aware spatial agreement while also producing the lowest SAL and distance error. By contrast, DAALL improved hit rate but did not improve FSS or object structure, reinforcing the need to interpret overlap-based metrics together with morphology and displacement diagnostics.

Overall, the object-based verification demonstrates that data assimilation improved selected aspects of hail-producing storm representation, but the improvement depended strongly on observation type and verification metric. Radar reflectivity assimilation provided the best balance between structural realism and spatial placement, whereas all-source assimilation increased areal coverage at the expense of object compactness and morphology. These results show that higher hit rate alone is not sufficient evidence of better hail-related representation, particularly for localized hazardous tropical convection associated with surface-reaching hail.

4. Discussion

4.1 Surface-Reaching Hail as a Manifestation of Hazardous Tropical Convection

The occurrence of surface-reaching hail over Yogyakarta is physically significant because the storm developed in a tropical environment with a high freezing level and a deep warm layer. Under such conditions, falling ice particles are expected to experience substantial melting before reaching the ground, making surface-reaching hail relatively rare in tropical environments [1], [3]–[5], [11]. Therefore, the presence of hail at the surface can be interpreted as a manifestation of hazardous tropical convection, because the parent storm was not merely ice-producing aloft but sufficiently intense to support hailstone growth, mixed-phase hydrometeor loading, and rapid downward transport through the melting layer [12]–[14], [48].

The combined observational evidence supports this interpretation. Radar observations showed that the strongest reflectivity and hail-likelihood signatures occurred during 08:00–08:20 UTC, closely bracketing the reported hail time. High radar reflectivity in deep convection is commonly associated with intense precipitation-sized hydrometeors, although it cannot uniquely distinguish hail from heavy rain or graupel without supporting evidence [27], [58], [87], [88]. Himawari-9 observations indicated rapid cloud-top cooling from approximately −53°C to −72°C within about 20 min, suggesting vigorous vertical cloud growth and strong updraft development. Similar satellite-based indicators have been widely used to diagnose rapid convective deepening and severe convective development [42], [60], [65], [72], [76]. The environmental analysis further showed moderate-to-strong instability, weak inhibition, low cloud base, and organized low-level convergence near the event region, consistent with atmospheric conditions favorable for deep moist convection and severe storm development [77], [78], [80], [82]. Together, these features indicate that the hail event was associated with a short-lived but intense convective core.

The kinematic setting suggests that this event was not controlled by a classic mid-latitude supercell pathway. The 0–6 km shear of approximately 16 m s^{-1} and 0–3 km shear of approximately 8 m s^{-1} indicate weak-to-moderate storm organization potential. This differs from many mid-latitude hailstorms, which are frequently linked to stronger vertical wind shear, organized rotating updrafts, and supercell-like dynamics [10], [11]. Thus, the Yogyakarta hail event is better interpreted as a tropical severe-convection case in which localized convergence

and rapid instability release produced an intense, compact updraft capable of generating hail-supporting mixed-phase processes [1], [3], [47].

This interpretation has important implications for hail prediction in humid tropical regions. Surface-reaching hail should not be inferred from high reflectivity alone, because intense tropical rainfall can also produce strong radar echoes. Instead, it should be diagnosed using converging evidence from surface reports, radar intensity and morphology, satellite-observed convective deepening, environmental constraints, and model-based hail-supporting proxies [17], [19], [23], [24], [61]. In this study, the coherence among these independent indicators strengthens the interpretation that the observed hail was produced by an unusually vigorous tropical convective cell.

4.2 Role of Radar Reflectivity Assimilation in Improving Storm Representation

The verification results indicate that radar reflectivity assimilation provided the most consistent improvement in representing the hail-producing convective storm. The DARFL experiment produced the lowest total SAL value and the lowest distance error among all experiments, indicating better agreement with the observed storm-object morphology and placement. This improvement is physically reasonable because radar reflectivity directly constrains precipitation-sized hydrometeors and convective-core intensity, which are central to the representation of hail-supporting convection [24], [27], [52], [53].

The improvement of DARFL over NODA was modest in absolute metric values, particularly for IoU and FSS. This suggests that radar reflectivity assimilation improved storm-object placement and morphology, but did not fully resolve the spatial mismatch between simulated and observed convective cores. Therefore, the value of DARFL should be interpreted as a physically consistent improvement in compact storm-core representation rather than evidence of deterministic surface-hail prediction skill.

In contrast, radial-velocity assimilation primarily constrains the storm-scale wind field and kinematic structure. Although this information is important for storm organization, its impact on hydrometeor loading and reflectivity morphology is indirect. This may explain why DAV and DARFLRV did not outperform DARFL in the object-based verification. For this event, correcting the hydrometeor and precipitation structure appears to have been more important than adjusting the wind field alone, particularly because hail-supporting convection depends strongly on mixed-phase hydrometeor growth, precipitation loading, and storm-core intensity [13], [43], [48], [49].

The DARFL experiment also produced a hail-supporting proxy footprint that was more spatially consistent with the radar-derived hail-likelihood object and the surface hail-report corridor. This suggests that reflectivity assimilation improved not only the simulated storm location, but also the representation of intense hydrometeor concentrations associated with hail-supporting convection. However, the improvement should be interpreted as enhanced representation of hail-supporting storm structure, not as direct prediction of surface hail occurrence, because radar reflectivity and model-derived hydrometeor proxies cannot uniquely confirm hail reaching the surface without independent surface evidence [58], [59], [61], [88].

These findings highlight the value of radar reflectivity assimilation for short-range prediction of localized tropical severe convection. In humid tropical environments, where surface-reaching hail is rare and highly localized, improving the structure and placement of compact convective cores may be more important than increasing the overall convective coverage. Therefore, radar reflectivity assimilation provides a particularly relevant observational constraint for modeling hail-supporting tropical convection, especially when evaluated using object-based metrics that account for storm morphology, amplitude, and spatial displacement [75], [85], [86].

4.3 Why All-Source Assimilation Did Not Necessarily Improve Storm Representation

The DAALL experiment demonstrates that assimilating more observation types does not automatically produce the most realistic convective-scale simulation. Although DAALL achieved the highest hit rate, it also produced the largest total SAL value, indicating that improved areal coverage was accompanied by an overexpanded or structurally distorted storm object. This finding is consistent with previous studies emphasizing that convective-scale forecast improvement depends not only on the amount of assimilated information, but also on whether the assimilated observations constrain the most relevant storm-scale processes [17], [19], [23], [53].

This result reflects an important limitation in convective-scale data assimilation. Different observation types constrain different parts of the atmospheric state. Radar reflectivity directly modifies hydrometeor and precipitation structures, radial velocity constrains wind fields, satellite observations influence cloud-field representation, and conventional observations adjust the broader thermodynamic and kinematic environment [24], [27], [52], [65]. When these constraints are combined, the resulting analysis may increase storm coverage without necessarily improving the compact structure of the hail-producing core.

For localized tropical hail, this distinction is critical. Surface-reaching hail depends on a compact region of intense mixed-phase microphysics, strong updrafts, hydrometeor loading, and rapid descent through the warm layer [11], [13], [43], [48]. A simulation that produces broad convection may overlap the observed hail area and

obtain a high hit rate, but it may still fail to represent the actual storm morphology required for hail production. Therefore, overlap-based improvement alone should not be interpreted as better hail-related storm representation.

The DAALL result reinforces the importance of object-based verification. Metrics such as hit rate and areal overlap can favor broad simulated objects, whereas SAL and distance error penalize structural distortion and displacement. Previous object-based verification studies have similarly shown that morphology, amplitude, and location errors are essential for evaluating convective-scale forecast quality, especially when small displacement errors or excessive spatial coverage can distort traditional grid-point scores [74], [75], [85], [86]. In this case, DARFL provided a better balance between object compactness, morphology, and spatial placement, while DAALL improved areal coverage at the expense of storm-object realism. This shows that the best assimilation strategy for tropical hail-related storm representation should be selected based on physically meaningful storm-object behavior, not simply on the number of assimilated observations.

4.4 Implications for Hazardous Tropical Convection Monitoring and Hail Nowcasting

The results have important implications for understanding and monitoring hazardous tropical convection associated with surface-reaching hail. First, the event demonstrates that hail-related storm monitoring depends not only on identifying deep convection, but also on resolving compact, rapidly intensifying convective cores. The Yogyakarta hail event occurred within a short temporal window, with the strongest radar hail-likelihood signatures appearing mainly between 08:00 and 08:20 UTC. This indicates that operational monitoring and nowcasting require high-frequency observations and short-range model guidance capable of capturing storm-scale evolution within tens of minutes [42], [60], [65], [76].

Second, the findings suggest that radar reflectivity assimilation can provide valuable short-range improvement when the target hazard is associated with localized hydrometeor loading and intense precipitation cores. In this case, DARFL improved storm-object morphology and placement more consistently than other assimilation configurations. For operational nowcasting, this means that radar reflectivity assimilation may be particularly useful for identifying where compact hail-supporting convective structures associated with hazardous tropical convection are most likely to develop, especially when combined with surface reports and satellite cloud-top cooling diagnostics [24], [27], [52], [53].

Third, the results show that broader convective coverage should not be interpreted as better representation of hail-related hazardous convection. DAALL produced the highest hit rate but also the poorest total SAL score, indicating that it overexpanded the simulated storm object. This is operationally important because an overexpanded hail-supporting forecast area may increase false alarms and reduce the practical value of warnings. For localized hazards such as tropical surface hail, storm-object quality should therefore be evaluated using storm-object realism, not only areal overlap [24], [27], [52], [53], [74], [75], [85], [86].

Fourth, satellite observations remain useful for diagnosing rapid convective deepening, particularly where radar coverage is limited or affected by sampling geometry. In this event, Himawari-9 captured rapid cloud-top cooling prior to the reported hail occurrence, providing early evidence of intensifying convection. However, satellite information should be interpreted as a cloud-top and vertical-growth indicator rather than as a direct hail-detection tool [38], [42], [67], [72].

Overall, the study suggests that a practical tropical hail nowcasting framework should combine surface reports, radar reflectivity evolution, satellite-observed cloud-top cooling, environmental convergence diagnostics, and convection-permitting model output. For operational use, the most valuable prediction target may not be deterministic surface hail occurrence, but the identification of compact hail-supporting convective objects that coincide with favorable environmental and observational signals [17], [19], [23], [24], [61].

4.5 Limitations and Future Work

Several limitations should be considered when interpreting the results. First, this study is based on a single surface-reaching hail event. Although the Yogyakarta case provides valuable evidence of hail-producing convection in a humid tropical environment, the findings should be interpreted as case-based evidence rather than a general conclusion for all tropical hailstorms. Additional events across different seasons, locations, and storm environments are required to evaluate whether the relative performance of the data assimilation experiments remains consistent [1], [3], [5], [11].

Second, the surface hail reports were derived from community-based and agency-based information rather than systematic hail-pad observations or instrumented hail-size measurements. These reports provide direct evidence that hail reached the ground, but they contain uncertainty in exact timing, location, and hailstone size. The use of a spatio-temporal matching window and location buffer reduces this uncertainty, but it cannot fully replace standardized hail observations or remote-sensing-based hail detection approaches [56], [59], [61].

Third, the synthetic reflectivity-based hail-supporting proxy is an empirical diagnostic rather than a physically explicit hail model. It identifies storm regions with strong hydrometeor loading and reflectivity characteristics favorable for hail-supporting convection, but does not simulate hailstone size distribution, melting during descent, fall trajectories, downdraft strength, or surface hail intensity. Therefore, the proxy should be

interpreted as an indicator of hail-supporting convection, not as a deterministic prediction of surface hailfall [48], [49], [89].

Fourth, the radar-based hail-likelihood thresholds and the WRF-derived hail-supporting proxy were empirically tuned for this event using the available surface hail reports and storm evolution. Because the tuning process was not designed as an independent sensitivity experiment, the resulting thresholds should not be generalized without further testing. Future work should conduct systematic threshold-sensitivity experiments, including ±5 dBZ perturbations and independent validation against additional tropical hail events.

Fifth, radar sampling uncertainty may affect the interpretation of the observed convective core. The Yogyakarta hail-report cluster was located approximately 84 km from the Semarang radar, with the lowest 0.5° beam sampling the storm at approximately 1.0 km above mean sea level. Although this sampling height is still useful for diagnosing lower-to-mid convective structure, beam broadening, attenuation, and range-related sampling effects may influence the observed reflectivity magnitude and object morphology [17], [24], [27], [87].

Finally, the verification results are sensitive to threshold selection, object definition, spatial smoothing, regridding, and masking procedures. Different reflectivity thresholds or object-identification criteria may alter the magnitude of SAL, IoU, FSS, and hit-rate values. For this reason, the study emphasizes relative comparison among experiments and multi-metric interpretation rather than reliance on a single verification score [74], [85], [86].

The assimilation design used a single analysis time followed by model spin-up before the peak hail-producing phase. This configuration is suitable for event-scale storm reconstruction and intercomparison among assimilation experiments, but it does not represent a rapid-update convective nowcasting cycle. Future studies should examine whether cycling radar assimilation closer to storm initiation and maturation further improves compact storm-core representation.

Future work should extend this framework to a larger sample of tropical hail events, incorporate more robust hail observations, and test additional microphysics and data assimilation configurations. Sensitivity experiments using different hail-proxy thresholds, microphysical schemes, and radar-assimilation settings would help determine the robustness of the present findings [43], [45], [46], [55]. Further development of physically based hail diagnostics, including melting-layer effects and hailstone survival probability, would also improve the representation of surface-reaching hail in tropical convection-permitting models [11], [13], [48].

5. Conclusions

This study examined hazardous tropical convection producing surface-reaching hail over Yogyakarta, Indonesia, on 11 March 2025. The event developed in a tropical environment characterized by moderate-to-strong instability, weak convective inhibition, a low lifting condensation level, a high freezing level, and organized low-level convergence. Under these conditions, the occurrence of surface-reaching hail indicates an unusually intense convective core capable of supporting mixed-phase hydrometeor growth and rapid downward transport through a deep warm layer.

Multi-source observations revealed that the hail event occurred during a brief period of rapid convective intensification. Radar observations showed that the strongest reflectivity and hail-likelihood signatures occurred between 08:00 and 08:20 UTC, closely coinciding with the reported hail occurrence at approximately 08:15 UTC. Himawari-9 observations further indicated rapid cloud-top cooling from approximately −53°C to −72°C within about 20 min, confirming rapid vertical cloud development before and during the hail-producing phase.

The assimilation experiments demonstrated that model improvement was strongly metric-dependent. Radar reflectivity assimilation produced the most balanced storm-object representation, yielding the lowest total SAL score and distance error. In contrast, all-source assimilation increased the simulated convective area but degraded object compactness. This contrast indicates that higher spatial overlap or hit rate alone is insufficient for evaluating localized hail-supporting convection.

The synthetic reflectivity-based hail-supporting proxy further showed that improved overlap with the reported hail region does not necessarily indicate a better representation of hail-related storm structure. Simulations with excessively broad hail-supporting areas may achieve high hit rates while misrepresenting the compact storm morphology associated with surface-reaching hail. Therefore, object-based verification is essential for distinguishing meaningful improvements in storm-core placement and structure from broad but unrealistic convective coverage.

Overall, this study demonstrates that rare surface-reaching tropical hailstorms should be evaluated using an integrated process-based and object-based framework that links surface reports, multi-source observations, and WRF data assimilation experiments. For this high-impact case, radar reflectivity assimilation provided the most physically consistent improvement in representing the compact hail-supporting convective core associated with hazardous tropical convection. Nevertheless, these findings should be interpreted as case-based evidence. Further evaluations using additional tropical hail events are required to assess the robustness and general applicability of the proposed framework.

Statements and Declarations

Competing Interests

The authors declare that they have no competing interests.

Author Contributions

KDO: Data curation, data processing, formal analysis, investigation, visualization, and preparation of the initial draft. AM: Conceptualization, methodology, supervision, validation, interpretation of the results, manuscript structuring, writing, original draft preparation, writing, review and editing, and project administration. Both authors have read and approved the final version of the manuscript.

Funding:

This research did not receive funding.

Reference

[1] J. F. León-Cruz, E. Caetano, J. Cortés-Ramos, C. Domínguez, and J. M. R. Méndez-Pérez, "Thunderstorm and Hailstorm Environments in Mexico," *Int. J. Climatol.*, vol. 43, no. 10, pp. 4379–4395, 2023, doi: 10.1002/joc.8093.

[2] Q. F. Tut, T. Raupach, and A. S. Taschetto, "Links Between Hail Hazard and Climate Modes of Variability Across Australia," *Q. J. R. Meteorol. Soc.*, vol. 151, no. 770, 2025, doi: 10.1002/qj.4985.

[3] F. P. Sari and S. Lasher-Trapp, "Hailstorm Events Over a Maritime Tropical Region: Storm Environments and Characteristics," *J. Geophys. Res. Atmos.*, vol. 130, no. 10, 2025, doi: 10.1029/2024jd042718.

[4] H. Lemons, "Hail in High and Low Latitudes," *Bull. Am. Meteorol. Soc.*, vol. 23, no. 2, pp. 61–72, 1942, doi: 10.1175/1520-0477-23.2.61.

[5] E. M. Murillo, C. R. Homeyer, and J. T. Allen, "A 23-Year Severe Hail Climatology Using GridRad MESH Observations," *Mon. Weather Rev.*, vol. 149, no. 4, pp. 945–958, 2021, doi: 10.1175/mwr-d-20-0178.1.

[6] M. Zamuriano, A. Martynov, L. Panziera, and S. Brönnimann, "Characteristics of a Hailstorm Over the Andean La Paz Valley," 2019, doi: 10.5194/nhess-2019-27.

[7] H. Bechis *et al.*, "Environments Associated With Hail and Convectively Generated Damaging Wind Gusts in South America," *Q. J. R. Meteorol. Soc.*, vol. 151, no. 772, 2025, doi: 10.1002/qj.5029.

[8] U. Saha, V. S. Prasad, S. I. Rani, and J. P. George, "Rare Winter-thunderstorms With Hail Overnight 12/13 December 2019 Over Delhi and Its Vicinity: An Observational Study," *Weather*, vol. 80, no. 7, pp. 234–243, 2024, doi: 10.1002/wea.7653.

[9] G. Chen *et al.*, "Linking Ice-Phase Microphysics to Raindrop Characteristics in Deep Convection: A Warm-Sector Extreme Rainfall Case Study in Eastern China," *Earth Sp. Sci.*, vol. 10, no. 2, 2023, doi: 10.1029/2022ea002697.

[10] H. E. Brooks *et al.*, "A Century of Progress in Severe Convective Storm Research and Forecasting," *Meteorol. Monogr.*, vol. 59, pp. 18.1-18.41, 2019, doi: 10.1175/amsmonographs-d-18-0026.1.

[11] J. T. Allen *et al.*, "Understanding Hail in the Earth System," *Rev. Geophys.*, vol. 58, no. 1, 2020, doi: 10.1029/2019rg000665.

[12] J. Hubbert, V. N. Bringi, L. D. Carey, and S. Bolen, "CSU-CHILL Polarimetric Radar Measurements From a Severe Hail Storm in Eastern Colorado," *J. Appl. Meteorol.*, vol. 37, no. 8, pp. 749–775, 1998, doi: 10.1175/1520-0450(1998)037<0749:ccprmf>2.0.co;2.

[13] J. A. Milbrandt and M. K. Yau, "A Multimoment Bulk Microphysics Parameterization. Part III: Control Simulation of a Hailstorm," *J. Atmos. Sci.*, vol. 63, no. 12, pp. 3114–3136, 2006, doi: 10.1175/jas3816.1.

[14] H.-M. Lin and P. K. Wang, "A Numerical Study of Microphysical Processes in the 21 June 1991 Northern Taiwan Mesoscale Precipitation System," *Peanut Sci.*, vol. 8, no. 4, p. 385, 1997, doi: 10.3319/tao.1997.8.4.385(a).

[15] R. Cui *et al.*, "Exploring Hail and Lightning Diagnostics Over the Alpine-Adriatic Region in a Km-Scale Climate Model," *Weather Clim. Dyn.*, vol. 4, no. 4, pp. 905–926, 2023, doi: 10.5194/wcd-4-905-2023.

[16] M. J. Murphy, J. S. Haase, R. Padullés, S. Chen, and M. Morris, "The Potential for Discriminating Microphysical Processes in Numerical Weather Forecasts Using Airborne Polarimetric Radio Occultations," *Remote Sens.*, vol. 11, no. 19, p. 2268, 2019, doi: 10.3390/rs11192268.

[17] S. Trömel *et al.*, "Overview: Fusion of Radar Polarimetry and Numerical Atmospheric Modelling Towards an Improved Understanding of Cloud and Precipitation Processes," 2021, doi: 10.5194/acp-2021-346.

[18] S. Khodayar *et al.*, "Overview Towards Improved Understanding of the Mechanisms Leading to Heavy Precipitation in the Western Mediterranean: Lessons Learned From HyMeX," 2021, doi: 10.5194/acp-2021-350.

[19] J. M. Fritsch *et al.*, "Quantitative Precipitation Forecasting: Report of the Eighth Prospectus Development

Team, U.S. Weather Research Program," *Bull. Am. Meteorol. Soc.*, vol. 79, no. 2, pp. 285–299, 1998, doi: 10.1175/1520-0477(1998)079<0285:qpfrot>2.0.co;2.
[20] H. Konow *et al.*, "Eurec ⁴ A's <i>HALO</I>," *Earth Syst. Sci. Data*, vol. 13, no. 12, pp. 5545–5563, 2021, doi: 10.5194/essd-13-5545-2021.
[21] R. Pincus *et al.*, "Observations From the NOAA P-3 Aircraft During ATOMIC," *Earth Syst. Sci. Data*, vol. 13, no. 7, pp. 3281–3296, 2021, doi: 10.5194/essd-13-3281-2021.
[22] J. Vivekanandan *et al.*, "The Next Generation Airborne Polarimetric Doppler Weather Radar," 2014, doi: 10.5194/gid-4-1-2014.
[23] W. F. Dabberdt and T. Schlatter, "Research Opportunities From Emerging Atmospheric Observing and Modeling Capabilities," *Bull. Am. Meteorol. Soc.*, vol. 77, no. 2, pp. 305–323, 1996, doi: 10.1175/1520-0477(1996)077<0305:rofeao>2.0.co;2.
[24] T. Matsui *et al.*, "Systematic Validation of Ensemble Cloud-Process Simulations Using Polarimetric Radar Observations and Simulator Over the NASA Wallops Flight Facility," *J. Geophys. Res. Atmos.*, vol. 128, no. 16, 2023, doi: 10.1029/2022jd038134.
[25] P. Kollias *et al.*, "Science Applications of Phased Array Radars," *Bull. Am. Meteorol. Soc.*, vol. 103, no. 10, pp. E2370–E2390, 2022, doi: 10.1175/bams-d-21-0173.1.
[26] B. Stevens *et al.*, "Eurec ⁴ A," *Earth Syst. Sci. Data*, vol. 13, no. 8, pp. 4067–4119, 2021, doi: 10.5194/essd-13-4067-2021.
[27] A. V Ryzhkov, J. C. Snyder, J. T. Carlin, A. Хаин, and M. Pinsky, "What Polarimetric Weather Radars Offer to Cloud Modelers: Forward Radar Operators and Microphysical/Thermodynamic Retrievals," *Atmosphere (Basel).*, vol. 11, no. 4, p. 362, 2020, doi: 10.3390/atmos11040362.
[28] Y. Dufournet and H. W. J. Russchenberg, "Towards the Improvement of Cloud Microphysical Retrievals Using Simultaneous Doppler and Polarimetric Radar Measurements," 2011, doi: 10.5194/amtd-4-527-2011.
[29] M. Mech *et al.*, "PAMTRA 1.0: A Passive and Active Microwave Radiative TRAnsfer Tool for Simulating Radiometer and Radar Measurements of the Cloudy Atmosphere," 2020, doi: 10.5194/gmd-2019-356.
[30] M. Mech *et al.*, "PAMTRA 1.0: The Passive and Active Microwave Radiative TRAnsfer Tool for Simulating Radiometer and Radar Measurements of the Cloudy Atmosphere," *Geosci. Model Dev.*, vol. 13, no. 9, pp. 4229–4251, 2020, doi: 10.5194/gmd-13-4229-2020.
[31] S. Bony *et al.*, "EUREC4A: A Field Campaign to Elucidate the Couplings Between Clouds, Convection and Circulation," pp. 357–396, 2017, doi: 10.1007/978-3-319-77273-8_16.
[32] M. Armon, F. Marra, Y. Enzel, D. Rostkier-Edelstein, and E. Morin, "Characterising Patterns of Heavy Precipitation Events in the Eastern Mediterranean Using a Weather Radar and Convection-Permitting WRF Simulations," 2019, doi: 10.5194/hess-2019-500.
[33] V. Bringi and D. S. Zrnić, "Polarization Weather Radar Development From 1970–1995: Personal Reflections," *Atmosphere (Basel).*, vol. 10, no. 11, p. 714, 2019, doi: 10.3390/atmos10110714.
[34] B. Utsav, S. M. Deshpande, S. K. Das, G. Pandithurai, and D. Niyogi, "Observed Vertical Structure of Convection During Dry and Wet Summer Monsoon Epochs Over the Western Ghats," *J. Geophys. Res. Atmos.*, vol. 124, no. 3, pp. 1352–1369, 2019, doi: 10.1029/2018jd028960.
[35] L. Bai, G. Chen, and L. Huang, "Image Processing of Radar Mosaics for the Climatology of Convection Initiation in South China," *J. Appl. Meteorol. Climatol.*, vol. 59, no. 1, pp. 65–81, 2020, doi: 10.1175/jamc-d-19-0081.1.
[36] Z. Chen, "Summer Surface Rainfall Deviations From Convective Cold-Cloud Shields Over China," *Geophys. Res. Lett.*, 2025, doi: 10.1029/2025gl117889.
[37] M. V YOUNG, G. A. MONK, and K. A. Browning, "Interpretation of Satellite Imagery of a Rapidly Deepening Cyclone," *Q. J. R. Meteorol. Soc.*, 1987, doi: 10.1256/smsqj.47802.
[38] J. Molinari and D. Vollaro, "Rapid Intensification of a Sheared Tropical Storm," *Mon. Weather Rev.*, 2010, doi: 10.1175/2010mwr3378.1.
[39] Y.-C. Liu, S. Chen, and F.-C. Chien, "Impact of MODIS and AIRS Total Precipitable Water on Modifying the Vertical Shear and Hurricane Emily Simulations," *J. Geophys. Res. Atmos.*, 2011, doi: 10.1029/2010jd014528.
[40] C. Liu, J. P. Punay, C. Wu, K. Chung, and P. Aryastana, "Characteristics of Deep Convective Clouds, Precipitation, and Cloud Properties of Rapidly Intensifying Tropical Cyclones in the Western North Pacific," *J. Geophys. Res. Atmos.*, 2022, doi: 10.1029/2022jd037328.
[41] C. P. Lackner *et al.*, "Insights Into the Relation Between Vertical Cloud Structure and Dynamics of Three Polar Lows: Observations From COMBLE," *Q. J. R. Meteorol. Soc.*, 2023, doi: 10.1002/qj.4543.
[42] Y. Zhang and X. Ni, "Cloud Properties in Hailstorms Over the Contiguous United States: A Perspective From GOES Advanced Baseline Imager's One-Min Rapid Scan," *J. Geophys. Res. Atmos.*, 2025, doi: 10.1029/2024jd042711.

[43] H. Morrison and J. A. Milbrandt, “Comparison of Two-Moment Bulk Microphysics Schemes in Idealized Supercell Thunderstorm Simulations,” *Mon. Weather Rev.*, vol. 139, no. 4, pp. 1103–1130, 2011, doi: 10.1175/2010mwr3433.1.
[44] W. Tao and M. W. Moncrieff, “Multiscale Cloud System Modeling,” *Rev. Geophys.*, vol. 47, no. 4, 2009, doi: 10.1029/2008rg000276.
[45] Y. Zhu, A. Zhou, K. Zhao, Y. Lu, and H. Huang, “The Observed and Simulated Evolution of a Microburst Using X-Band Phased-Array Radar Data Assimilation With EnKF,” *J. Geophys. Res. Atmos.*, vol. 130, no. 1, 2024, doi: 10.1029/2024jd042614.
[46] Z. Cheng and X. Liu, “A Numerical Simulation of Convective Systems in Southeast China: A Comparison of Microphysical Schemes and Sensitivity Experiments on Raindrop Break and Evaporation,” *Remote Sens.*, vol. 16, no. 22, p. 4297, 2024, doi: 10.3390/rs16224297.
[47] F. P. Sari, I. Manola, A. Tsiringakis, and G. Steeneveld, “Understanding the Role of Sea Surface Temperature and Urbanization on Severe Thunderstorms Dynamics: A Case Study in Surabaya, Indonesia,” *J. Geophys. Res. Atmos.*, vol. 128, no. 17, 2023, doi: 10.1029/2023jd038817.
[48] K. G. Kacan and Z. J. Lebo, “Microphysical and Dynamical Effects of Mixed-Phase Hydrometeors in Convective Storms Using a Bin Microphysics Model: Melting,” *Mon. Weather Rev.*, vol. 147, no. 12, pp. 4437–4460, 2019, doi: 10.1175/mwr-d-18-0032.1.
[49] L. Luo, M. Xue, K. Zhu, and B. Zhou, “Explicit Prediction of Hail Using Multimoment Microphysics Schemes for a Hailstorm of 19 March 2014 in Eastern China,” *J. Geophys. Res. Atmos.*, vol. 122, no. 14, pp. 7560–7581, 2017, doi: 10.1002/2017jd026747.
[50] H. M. Mallinson and S. Lasher-Trapp, “An Investigation of Hydrometeor Latent Cooling Upon Convective Cold Pool Formation, Sustainment, and Properties,” *Mon. Weather Rev.*, vol. 147, no. 9, pp. 3205–3222, 2019, doi: 10.1175/mwr-d-18-0382.1.
[51] L. Liu, C. Lin, Y. Bai, and D. He, “Assessing the Effects of Microphysical Scheme on Convective and Stratiform Characteristics in a Mei-Yu Rainfall Combining WRF Simulation and Field Campaign Observations,” *Adv. Meteorol.*, vol. 2020, pp. 1–17, 2020, doi: 10.1155/2020/8231320.
[52] J. T. Carlin, J. Gao, J. C. Snyder, and A. V Ryzhkov, “Assimilation of ZDR Columns for Improving the Spinup and Forecast of Convective Storms in Storm-Scale Models: Proof-of-Concept Experiments,” *Mon. Weather Rev.*, vol. 145, no. 12, pp. 5033–5057, 2017, doi: 10.1175/mwr-d-17-0103.1.
[53] G. Zhang *et al.*, “Current Status and Future Challenges of Weather Radar Polarimetry: Bridging the Gap Between Radar Meteorology/Hydrology/Engineering and Numerical Weather Prediction,” *Adv. Atmos. Sci.*, vol. 36, no. 6, pp. 571–588, 2019, doi: 10.1007/s00376-019-8172-4.
[54] W. Tao *et al.*, “Relating Vertical Velocity and Cloud/Precipitation Properties: A Numerical Cloud Ensemble Modeling Study of Tropical Convection,” *J. Adv. Model. Earth Syst.*, vol. 14, no. 9, 2022, doi: 10.1029/2021ms002677.
[55] M. Johnson, M. Xue, and Y. Jung, “Biases and Skill of Four Two-Moment Bulk Microphysics Schemes in Convection-Allowing Forecasts for the 2018 Hazardous Weather Testbed Spring Forecasting Experiment Period,” *Weather Forecast.*, vol. 38, no. 9, pp. 1621–1642, 2023, doi: 10.1175/waf-d-22-0171.1.
[56] H. J. Punge, K. M. Bedka, M. Kunz, S. D. Bang, and K. F. Itterly, “Characteristics of Hail Hazard in South Africa Based on Satellite Detection of Convective Storms,” *Nat. Hazards Earth Syst. Sci.*, 2023, doi: 10.5194/nhess-23-1549-2023.
[57] M. R. Clark and J. D. Webb, “A Severe Hailstorm Across the English Midlands on 28 June 2012,” *Weather*, 2013, doi: 10.1002/wea.2162.
[58] R. Cică, S. Burcea, and R. Bojariu, “Assessment of Severe Hailstorms and Hail Risk Using Weather Radar Data,” *Meteorol. Appl.*, 2015, doi: 10.1002/met.1512.
[59] K. Mróz, A. Battaglia, T. J. Lang, D. J. Cecil, S. Tanelli, and F. Tridon, “Hail-Detection Algorithm for the GPM Core Observatory Satellite Sensors,” *J. Appl. Meteorol. Climatol.*, 2017, doi: 10.1175/jamc-d-16-0368.1.
[60] B. Z. Ribeiro *et al.*, “An Evaluation of the GOES-16 Rapid Scan for Nowcasting in Southeastern Brazil: Analysis of a Severe Hailstorm Case,” *Weather Forecast.*, 2019, doi: 10.1175/waf-d-19-0070.1.
[61] S. Laviola, G. Monte, V. Levizzani, R. Ferraro, and J. Beauchamp, “A New Method for Hail Detection From the GPM Constellation: A Prospect for a Global Hailstorm Climatology,” *Remote Sens.*, 2020, doi: 10.3390/rs12213553.
[62] A. Manzato, V. Riva, A. Tiesi, and M. M. Miglietta, “Observational Analysis and Simulations of a Severe Hailstorm in Northeastern Italy,” *Q. J. R. Meteorol. Soc.*, 2020, doi: 10.1002/qj.3886.
[63] F. Battaglioli, P. Groenemeijer, T. Púčik, M. Taszarek, U. Ulbrich, and H. W. Rust, “Modeled Multidecadal Trends of Lightning and (Very) Large Hail in Europe and North America (1950–2021),” *J. Appl. Meteorol. Climatol.*, 2023, doi: 10.1175/jamc-d-22-0195.1.
[64] A. Giordani *et al.*, “Characterizing Hail-Prone Environments Using Convection-Permitting Reanalysis

and Overshooting Top Detections Over South-Central Europe," 2023, doi: 10.5194/egusphere-2023-2639.
[65] Y. Lee, C. D. Kummerow, and M. Županski, "A Simplified Method for the Detection of Convection Using High-Resolution Imagery From GOES-16," *Atmos. Meas. Tech.*, 2021, doi: 10.5194/amt-14-3755-2021.
[66] Y. Lee, C. D. Kummerow, and M. Županski, "A Simplified Method for the Detection of Convection Using High Resolution Imagery From GOES-16," 2020, doi: 10.5194/amt-2020-38.
[67] E. M. Wilcox, T. Yuan, and H. Song, "Deep Convective Cloud System Size and Structure Across the Global Tropics and Subtropics," *Atmos. Meas. Tech.*, 2023, doi: 10.5194/amt-16-5387-2023.
[68] R. Stenz, X. Dong, B. Xi, Z. Feng, and R. J. Kuligowski, "Improving Satellite Quantitative Precipitation Estimation Using GOES-Retrieved Cloud Optical Depth," *J. Hydrometeorol.*, 2016, doi: 10.1175/jhm-d-15-0057.1.
[69] F. Cutraro, V. S. Galligani, and Y. G. Skabar, "Evaluation of Synthetic Satellite Images Computed From Radiative Transfer Models Over a Region of South America Using WRF and GOES-13/16 Observations," *Q. J. R. Meteorol. Soc.*, 2021, doi: 10.1002/qj.4111.
[70] G. Hong, G. Heygster, and C. A. Morales, "Effect of Cirrus Clouds on the Diurnal Cycle of Tropical Deep Convective Clouds," *J. Geophys. Res. Atmos.*, 2006, doi: 10.1029/2005jd006208.
[71] G. Lu, Y. Ren, S. Fu, and H. Xue, "Statistics of Isolated Deep Convection Initiation and Its Relation to Topography in the North China Area," *J. Geophys. Res. Atmos.*, 2023, doi: 10.1029/2022jd037949.
[72] K. Khlopenkov, K. M. Bedka, J. W. Cooney, and K. F. Itterly, "Recent Advances in Detection of Overshooting Cloud Tops From Longwave Infrared Satellite Imagery," *J. Geophys. Res. Atmos.*, 2021, doi: 10.1029/2020jd034359.
[73] S. A. Taylor, P. Stier, B. White, S. Finkensieper, and M. Stengel, "Evaluating the Diurnal Cycle in Cloud Top Temperature From SEVIRI," 2016, doi: 10.5194/acp-2016-878.
[74] F. Senf, D. Klocke, and M. Brueck, "Size-Resolved Evaluation of Simulated Deep Tropical Convection," *Mon. Weather Rev.*, 2018, doi: 10.1175/mwr-d-17-0378.1.
[75] M. Rempel, F. Senf, and H. Deneke, "Object-Based Metrics for Forecast Verification of Convective Development With Geostationary Satellite Data," *Mon. Weather Rev.*, 2017, doi: 10.1175/mwr-d-16-0480.1.
[76] C. C. Henken, M. Schmeits, H. Deneke, and R. Roebeling, "Using MSG-SEVIRI Cloud Physical Properties and Weather Radar Observations for the Detection of Cb/TCu Clouds," *J. Appl. Meteorol. Climatol.*, 2011, doi: 10.1175/2011jamc2601.1.
[77] A. Madhulatha *et al.*, "Climatology of Thermodynamic Indices and Background Synoptic Conditions Responsible for Severe Convection During Pre- to Post-monsoon Seasons Over Indian Region," *Int. J. Climatol.*, 2024, doi: 10.1002/joc.8471.
[78] D. L. Arnold, "Severe Deep Moist Convective Storms: Forecasting and Mitigation," *Geogr. Compass*, 2007, doi: 10.1111/j.1749-8198.2007.00069.x.
[79] J. R. Kulkarni *et al.*, "Unprecedented Hailstorms Over North Peninsular India During February–March 2014," *J. Geophys. Res. Atmos.*, 2015, doi: 10.1002/2015jd023093.
[80] D. Suárez-Molina, S. Fernández-González, J. C. Suárez González, and A. Oliver, "Analysis of Sounding Derived Parameters and Application to Severe Weather Events in the Canary Islands," *Atmos. Res.*, 2020, doi: 10.1016/j.atmosres.2020.104865.
[81] D. Wang *et al.*, "An Observational Comparison of Level of Neutral Buoyancy and Level of Maximum Detrainment in Tropical Deep Convective Clouds," *J. Geophys. Res. Atmos.*, 2020, doi: 10.1029/2020jd032637.
[82] J. Zhang, J. Guo, J. Li, J. Shao, B. Tong, and S. Zhang, "The Prestorm Environment and Prediction for Local- and Nonlocal-Scale Precipitation: Insights Gained From High-Resolution Radiosonde Measurements Across China," *J. Geophys. Res. Atmos.*, 2022, doi: 10.1029/2021jd036395.
[83] H. Morrison, "On the Robustness of Aerosol Effects on an Idealized Supercell Storm Simulated With a Cloud System-Resolving Model," 2012, doi: 10.5194/acpd-12-10493-2012.
[84] D. Lagomarsino *et al.*, "Quantitative Comparison Between Two Different Methodologies to Define Rainfall Thresholds for Landslide Forecasting," 2015, doi: 10.5194/nhessd-3-891-2015.
[85] M. Hallerstig, M. Køltzow, and S. Mayer, "Developing a Methodology for User-oriented Verification of Polar Low Forecasts," *Q. J. R. Meteorol. Soc.*, vol. 150, no. 764, pp. 4348–4370, 2024, doi: 10.1002/qj.4819.
[86] E. García-Ortega, A. Navarro, F. J. Tapiador, J. L. Sánchez, and A. Merino, "Evaluation of WRF Model Performance for Hailstorms in Southern France Using DPR-GPM Data," *J. Geophys. Res. Atmos.*, vol. 130, no. 19, 2025, doi: 10.1029/2025jd043462.
[87] V. Bringi and D. S. Zrnić, "Role of Electromagnetics in Polarization Radar Development From 1970-1995: Personal Reflections," 2019, doi: 10.20944/preprints201910.0197.v2.
[88] S. Ștefan and N. Barbu, "Radar-derived Parameters in Hail-producing Storms and the Estimation of Hail

Occurrence in Romania Using a Logistic Regression Approach," *Meteorol. Appl.*, 2018, doi: 10.1002/met.1726.

[89] H. Morrison, J. A. Milbrandt, G. H. Bryan, K. Ikeda, S. A. Tessendorf, and G. Thompson, "Parameterization of Cloud Microphysics Based on the Prediction of Bulk Ice Particle Properties. Part II: Case Study Comparisons With Observations and Other Schemes," *J. Atmos. Sci.*, 2015, doi: 10.1175/jas-d-14-0066.1.